Biogeosciences, 21, 3215–3238, 2024
https://doi.org/10.5194/bg-21-3215-2024

Biogeosciences Open Access EGU

Isotopomer labeling and oxygen dependence of hybrid nitrous oxide production

Colette L. Kelly[1,2], Nicole M. Travis[1], Pascale Anabelle Baya[1], Claudia Frey[3], Xin Sun[4], Bess B. Ward[5], and Karen L. Casciotti[1,6]

[1]Department of Earth System Science, Stanford University, Stanford, CA 94305, USA
[2]Department of Marine Chemistry and Geochemistry, Woods Hole Oceanographic Institution, Woods Hole, MA 02543, USA
[3]Department of Environmental Science, University of Basel, Basel, Switzerland
[4]Department of Global Ecology, Carnegie Institution for Science, Stanford, CA 94305, USA
[5]Department of Geosciences, Princeton University, Princeton, NJ 08544, USA
[6]Oceans Department, Stanford University, Stanford, CA 94305, USA

Correspondence: Colette L. Kelly (colette.kelly@whoi.edu)

Received: 9 November 2023 – Discussion started: 28 November 2023
Revised: 2 April 2024 – Accepted: 22 May 2024 – Published: 17 July 2024

Abstract. Nitrous oxide (N_2O) is a potent greenhouse gas and ozone depletion agent, with a significant natural source from marine oxygen-deficient zones (ODZs). Open questions remain, however, about the microbial processes responsible for this N_2O production, especially hybrid N_2O production when ammonia-oxidizing archaea are present. Using ^{15}N-labeled tracer incubations, we measured the rates of N_2O production from ammonium (NH_4^+), nitrite (NO_2^-), and nitrate (NO_3^-) in the eastern tropical North Pacific ODZ and the isotopic labeling of the central (α) and terminal (β) nitrogen (N) atoms of the N_2O molecule. We observed production of both doubly and singly labeled N_2O from each tracer, with the highest rates of labeled N_2O production at the same depths as the near-surface N_2O concentration maximum. At most stations and depths, the production of $^{45}N_2O^{\alpha}$ and $^{45}N_2O^{\beta}$ were statistically indistinguishable, but at a few depths there were significant differences in the labeling of the two nitrogen atoms in the N_2O molecule. Implementing the rates of labeled N_2O production in a time-dependent numerical model, we found that N_2O production from NO_3^- dominated at most stations and depths, with rates as high as 1600 ± 200 pM N_2O d^{-1}. Hybrid N_2O production, one of the mechanisms by which ammonia-oxidizing archaea produce N_2O, had rates as high as 230 ± 80 pM N_2O d^{-1} that peaked in both the near-surface and deep N_2O concentration maxima. Based on the equal production of $^{45}N_2O^{\alpha}$ and $^{45}N_2O^{\beta}$ in the majority of our experiments, we infer that hybrid N_2O production likely has a consistent site preference, despite drawing from two distinct substrate pools. We also found that the rates and yields of hybrid N_2O production were enhanced at low dissolved oxygen concentrations ($[O_2]$), with hybrid N_2O yields as high as 20 % at depths where $[O_2]$ was below detection (880 nM) but nitrification was still active. Finally, we identified a few incubations with $[O_2]$ up to 20 µM where N_2O production from NO_3^- was still active. A relatively high O_2 tolerance for N_2O production via denitrification has implications for the feedbacks between marine deoxygenation and greenhouse gas cycling.

1 Introduction

Nitrous oxide (N_2O) is one of the lesser-known greenhouse gases, yet its potential to warm the environment on a per-molecule basis is immense. N_2O has a global warming potential 273 times that of carbon dioxide (Smith et al., 2021), and its atmospheric mixing ratio is increasing at a rate of 0.85 ± 0.03 ppb yr^{-1} (Tian et al., 2020). In the ocean, hotspots of N_2O production and flux to the atmosphere occur in marine oxygen-deficient zones (ODZs), where steep redox gradients allow multiple N_2O production processes to overlap (Codispoti and Christensen, 1985). ODZs have expanded over the last 60 years (Breitburg et al., 2018; Stramma et al., 2008) and will likely continue to do so as the oceans warm

(Oschlies et al., 2018), although the fate of the anoxic cores of ODZs ($[O_2] \leq 20\,\mu mol\,kg^{-1}$) remains uncertain (Bianchi et al., 2018; Busecke et al., 2022; Cabré et al., 2015). Without a clear picture of N_2O cycling in these regions, it is impossible to predict how climate change will impact the marine emissions of this powerful greenhouse gas.

Much of the N_2O cycling in ODZs is linked to denitrification. In low-oxygen waters, denitrifying organisms produce N_2O as an intermediate during organic matter remineralization (Dalsgaard et al., 2014; Naqvi et al., 2000; Zumft, 1997). Both direct rate measurements (Frey et al., 2020; Ji et al., 2015, 2018) and natural abundance isotope measurements (Casciotti et al., 2018; Kelly et al., 2021; Monreal et al., 2022; Toyoda et al., 2023) indicate that N_2O production directly from nitrate (NO_3^-), i.e., without exchange with extracellular nitrite (NO_2^-) or nitric oxide (NO) pools, is the primary source of N_2O in ODZs. N_2O production from extracellular NO_2^-, meanwhile, tends to occur at lower rates (Frey et al., 2020; Ji et al., 2015, 2018). Historically, N_2O production from denitrification was thought to cease at dissolved oxygen concentrations above 2–3 µM (Dalsgaard et al., 2014), but more recent data suggest that N_2O production from NO_3^- can occur at ambient oxygen levels as high as 30 µM (Frey et al., 2020; Ji et al., 2018). N_2O consumption via denitrification is more sensitive to oxygen than N_2O production via denitrification, leading to an oxygen window in which denitrification is a source but not a sink of N_2O (Babbin et al., 2015; Dalsgaard et al., 2014; Farías et al., 2009; Frey et al., 2020), although the oxygen inhibition constant for N_2O consumption remains difficult to define (Sun et al., 2021a). N_2O may also be consumed through N_2O fixation, although the importance of N_2O fixation in the ocean has yet to be determined (Farías et al., 2013; Si et al., 2023).

Nonetheless, a significant fraction of the N_2O in the oxyclines above and below ODZs may be derived from archaeal nitrification. When NO_2^- is present, isotopic evidence continues to suggest that ammonia-oxidizing archaea can produce N_2O via a hybrid mechanism that combines nitrogen (N) derived from NO_2^- and ammonium (NH_4^+) to form the N_2O molecule (Frame et al., 2017; Frey et al., 2020, 2023; Stieglmeier et al., 2014; Trimmer et al., 2016). New evidence indicates that ammonia-oxidizing archaea can produce N_2O both as a by-product of hydroxylamine oxidation and via hybrid N_2O production and that the ratio of these processes depends on the ratio of NH_4^+ to NO_2^- available to the archaea (Wan et al., 2023b). The exact mechanism and enzymology of archaeal N_2O production remains unknown (Carini et al., 2018; Stein, 2019) but may involve a reaction between hydroxylamine and NO, which occur as intermediates during archaeal ammonia oxidation (Kozlowski et al., 2016; Lancaster et al., 2018; Martens-Habbena et al., 2015; Vajrala et al., 2013). In anaerobic conditions, ammonia-oxidizing archaea are also capable of NO dismutation to O_2 and N_2, which may involve N_2O as an intermediate (Kraft et al., 2022). Ammonia-oxidizing bacteria, more common in regions that are nutrient-replete, produce N_2O as a byproduct of hydroxylamine oxidation (Cohen and Gordon, 1979) and via nitrifier denitrification as oxygen concentrations decline (Goreau et al., 1980; Stein and Yung, 2003; Wrage et al., 2001) and nitrite concentrations rise (Frame and Casciotti, 2010).

The stable natural abundance nitrogen and oxygen isotopes of N_2O can provide quantification of – and distinction among – potential N_2O cycling mechanisms (Kim and Craig, 1990; Rahn and Wahlen, 2000; Toyoda and Yoshida, 1999). For example, natural abundance N_2O isotopocule studies have indicated that the high near-surface N_2O accumulations in the eastern tropical North Pacific (ETNP) ODZ are 80 % derived from denitrification and 20 % derived from nitrification (Kelly et al., 2021). The isotopic content of the individual N and oxygen (O) atoms in the N_2O molecule are expressed in delta notation, defined as $\delta(^{15}N)$ or $\delta(^{18}O) = (R_{sample}/R_{standard} - 1)$, where $R_{standard}$ for $\delta(^{15}N)$ and $R_{standard}$ for $\delta(^{18}O)$ are the ratios $^{15}N\,/\,^{14}N$ of air and $^{18}O\,/\,^{16}O$ of Vienna Standard Mean Ocean Water (VSMOW), respectively (Kim and Craig, 1990; Rahn and Wahlen, 2000; Toyoda and Yoshida, 1999). In addition to the bulk N and O isotope ratios in N_2O, we can measure the isotopic content of the inner (α) N atom and the outer (β) N atom in N_2O (Brenninkmeijer and Röckmann, 1999; Toyoda and Yoshida, 1999). The difference in the ^{15}N content of these two atoms is often referred to as the "site preference" and is defined as $\delta(^{15}N^{sp}) = \delta(^{15}N^{\alpha}) - \delta(^{15}N^{\beta})$. In natural abundance studies, $\delta(^{15}N^{sp})$ is particularly useful because it exhibits distinct values for different N_2O production processes, which are independent of the isotopic value of the substrate (Frame and Casciotti, 2010; Sutka et al., 2003, 2004, 2006; Toyoda et al., 2002, 2005). This allows partitioning between different N_2O sources and has been used extensively to quantify N_2O cycling in the ocean (Bourbonnais et al., 2017, 2023; Casciotti et al., 2018; Farías et al., 2009; Kelly et al., 2021; Monreal et al., 2022; Popp et al., 2002; Toyoda et al., 2002, 2005, 2019, 2021, 2023; Westley et al., 2006; Yamagishi et al., 2007). As we elaborate upon in the discussion, however, the premise that $\delta(^{15}N^{sp})$ exhibits a unique and consistent value depends on the assumption that both N atoms in N_2O are derived from a singular substrate pool. Thus, hybrid N_2O production may complicate traditional interpretations of natural abundance N_2O isotopocules.

Previous studies have used ^{15}N tracer experiments to measure N_2O production rates in ODZs (Frey et al., 2020, 2023; Ji et al., 2015, 2018). These studies used the accumulation of $^{45}N_2O$ and $^{46}N_2O$ resulting from the addition of ^{15}N-labeled substrates such as ^{15}N–NH_4^+ and ^{15}N–NO_2^- to measure N_2O production rates. To our knowledge, the isotopomer measurement has never been applied to ^{15}N tracer experiments to track ^{15}N from different substrates into the α and β positions of the N_2O molecule. Here, we present data showing the production of N_2O isotopomers with ^{15}N in the α position ($^{45}N_2O^{\alpha}$) and ^{15}N in the β position ($^{45}N_2O^{\beta}$) from

^{15}N-labeled NH_4^+, NO_2^-, and NO_3^-. Measuring the production of $^{45}N_2O^{\alpha}$ and $^{45}N_2O^{\beta}$ creates an additional constraint on N_2O production mechanisms and thus allows us to quantify different source processes more precisely and accurately. We employed these measurements to (a) validate previous ^{15}N tracer studies of N_2O production rates in the ETNP; (b) uncover that the hybrid pathway dominates production by nitrification; (c) establish the insignificance of production solely from NH_4^+ except the surface; and (d) infer a constant $\delta(^{15}N^{sp})$ for hybrid N_2O, despite drawing from two substrate pools. We also use these results to confirm inferences from natural abundance N_2O isotopocules measured in the same system (Kelly et al., 2021).

2 Methods

2.1 Sampling sites

Experiments were performed at three stations in the eastern tropical North Pacific on the R/V *Sally Ride* in March–April 2018 (Fig. 1). Station PS1 (10° N, 113° W) was on the edge of the oxygen-deficient region, station PS2 (16° N, 105° W) was near the geographic center of the ODZ, and station PS3 (18° N, 102° W) was 19 km from the coast of Mexico (Fig. 1). Samples were collected from 30 L Niskin bottles mounted on a 12-place rosette with a conductivity–temperature–depth profiler and sensors for chlorophyll *a* fluorescence and dissolved O_2 (Sea-Bird SBE 43 oxygen sensor). The cruise took place during a weak La Niña event (Ocean Niño Index = −0.6 °C; NOAA/National Weather Service, 2020).

Ambient [NO_2^-] and [NH_4^+] were measured shipboard with standard colorimetric (Grasshoff et al., 1999) and fluorometric methods (Grasshoff et al., 1999; Holmes et al., 1999), respectively. Ambient [NO_3^-] was measured at Stanford University using a Westco SmartChem 200 Discrete Analyzer (detection limit 83 nM, precision 0.6 µM). Ambient [N_2O] was measured via an isotope ratio mass spectrometer (IRMS) at the Stanford Stable Isotope Biogeochemistry Laboratory as part of a prior study (Kelly et al., 2021).

2.2 Sample collection

Incubation depths were chosen to target prominent hydrographic features: the primary NO_2^- maximum, shallow and deep oxyclines, oxic–anoxic interfaces above and below the ODZ, secondary chlorophyll *a* maximum, and secondary NO_2^- maximum (Table S1). Incubation samples were filled directly from Niskin bottles into 160 mL glass serum bottles (WHEATON) using Tygon tubing. Incubation bottles were overflowed three times before being capped and sealed bubble-free, with no headspace, using gray butyl rubber septa (National Scientific) and aluminum crimp seals. To minimize oxygen contamination during sampling, incubation bottles were overflowed in a secondary container filled with sub-

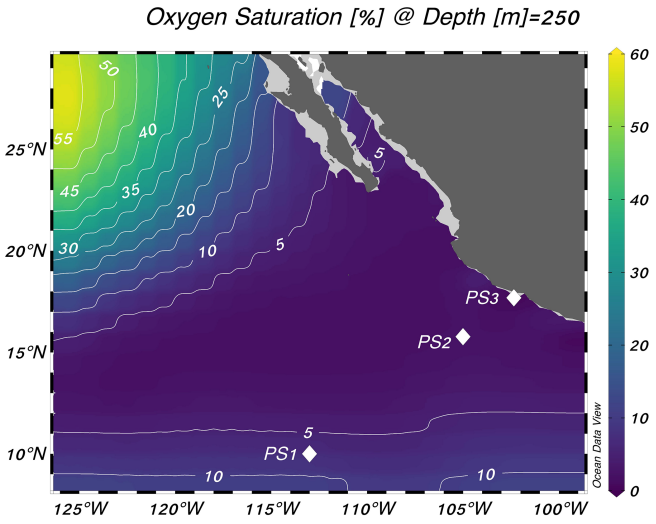

Figure 1. Locations of the three stations sampled for this study. Stations are plotted on top of World Ocean Atlas oxygen saturation (%) at 250 m depth (World Ocean Atlas, 2013). Schlitzer, Reiner, Ocean Data View, https://odv.awi.de, last access: 25 October 2023.

oxic water from the same depth, and Niskin bottles were vented with carbon dioxide gas to displace the withdrawn water. The butyl rubber stoppers were deoxygenated in a He-flushed anaerobic chamber for ∼ 1 week prior to sampling.

After sample collection, a 2 mL He headspace was created in each bottle by displacing the 2 mL sample from the bottle with He. At most (all but two) anoxic depths at stations PS2 and PS3, samples were sparged with He gas for 90 min at a flow rate of at least 100 mL min^{-1}, equivalent to 56 volume exchanges, to remove potential oxygen contamination introduced during sampling. Depths with low but non-zero ambient dissolved oxygen were not purged with He gas. After sparging, 100 µL of 1030 ppm N_2O in He (4 nmol N_2O) in gaseous form was introduced back into each bottle for a final concentration of 26 nM to provide a constant background of N_2O for later isotopic analysis (Fig. S4a). The isotopic content of this N_2O carrier, measured independently via IRMS (Kelly et al., 2023; McIlvin and Casciotti, 2010), was $\delta(^{15}N^{\alpha}) = -1.5 \pm 0.2$ ‰, $\delta(^{15}N^{\beta}) = 0.2 \pm 0.4$ ‰, $\delta(^{15}N^{bulk}) = -0.65 \pm 0.08$ ‰, and $\delta(^{18}O) = 37.4 \pm 0.3$ ‰.

Time series were constructed by sacrificing triplicate bottles over a time course, rather than by resampling the incubation bottles over time. A total of 27 incubation samples were thus produced at each experimental depth, comprised of triplicate samples for each of the three time points and three tracers. For each station and depth, nine samples were amended with $^{15}NH_4Cl$ (98.8 atm % ^{15}N; Sigma-Aldrich) to a final concentration of 0.501 µM and with $Na^{14}NO_2$ to a final concentration 1.01 µM. Nine samples were amended with $Na^{15}NO_2$ (98.8 atm % ^{15}N; Sigma-Aldrich) to a final concentration of 5.00 µM and with $^{14}NH_4Cl$ to a final concentra-

tion of 0.510 µM. Finally, nine samples were amended with $K^{15}NO_3$ (98.8 atm % ^{15}N; Sigma-Aldrich) to a final concentration of 1.00 µM, plus 1.01 µM $Na^{14}NO_2$ and 0.510 µM $^{14}NH_4Cl$. Note that the $Na^{15}NO_2$ tracer was added at a higher concentration than the other tracers or the $Na^{14}NO_2$ carrier; this discrepancy was due to a miscalculation that was caught midway through the cruise, but the high tracer addition was retained for the sake of consistency. The NO_2^- and NH_4^+ tracer and carrier additions were confirmed via $[NO_2^-]$ and $[NH_4^+]$ measurements of sample aliquoted from each bottle immediately before samples were measured for N_2O isotopic content, using colorimetric and fluorometric techniques (Grasshoff et al., 1999; Holmes et al., 1999). The $Na^{14}NO_2$ and $^{14}NH_4Cl$ amendments served two purposes: (1) to provide enough total NO_2^- for isotopic analysis of $^{15}NO_2^-$ produced from $^{15}NH_4^+$ and (2) to minimize isotope dilution of the substrate pool, which can cause underestimation of rates with low substrate additions. The final atm % ^{15}N of the substrate pools was thus 56 %–100 % for ^{15}N–NH_4^+, 65 %–100 % for ^{15}N–NO_2^-, and 2 %–92 % for ^{15}N–NO_3^- experiments. Three samples for each tracer were terminated immediately after tracer addition with the addition of 100 µL saturated mercuric chloride ($HgCl_2$) solution. These also served as abiotic controls. The remaining samples were incubated at 12 °C in the dark; three samples per tracer were terminated at 12 h and at 24 h with 100 µL saturated $HgCl_2$. All samples were incubated at 12 °C, which was chosen as an intermediate temperature that approximated subsurface conditions. After termination, samples were stored at room temperature (∼ 20 °C) in the dark until isotope analysis.

2.3 Chemiluminescent optode oxygen measurements

Eight 160 mL glass serum bottles were prepared with a chemiluminescent oxygen optode spot (PyroScience) affixed to the inner glass wall with silicone glue. These bottles were incubated alongside experimental bottles to monitor dissolved $[O_2]$ during incubations. At stations PS2 and PS3, two optode bottles per depth were filled, purged, amended with the N_2O carrier, and incubated without the addition of tracer or $HgCl_2$. At each time point, $[O_2]$ was measured in each sensor bottle for at least 10 min using fiber-optic cables paired to the oxygen optode spot mounted inside the bottle (PyroScience). The fiber-optic cables were calibrated with a two-point measurement of (1) a sodium sulfite solution (30 g L^{-1} in DI, or 0.24 M) and (2) surface seawater saturated with air at 12 °C (270 µM $[O_2]$, based on a salinity of 35 psu and a temperature of 12 °C) (Garcia and Gordon, 1992). The two calibration bottles, each containing its own optode spot, were used to calibrate all four of the fiber-optic cables, effectively correcting them to the same scale. Differences in detection limit between sensor spots were accounted for by first performing this two-point calibration procedure to correct for differences between fiber-optic cables and then by measuring the minimum oxygen concentration measured by each sensor spot in purged seawater (purged at 100 mL min^{-1}. for 90 min, equal to 56 volume exchanges). Those detection limits were specific to each optode spot and varied from 146–880 nM $[O_2]$.

The optode $[O_2]$ measurements were adjusted for the detection limit specific to each sensor spot; optode $[O_2]$ for each experiment was calculated as the mean measured $[O_2]$ at each of the three time points. No optode measurements were made at station PS1, since this station lacked a secondary NO_2^- maximum; thus incubations performed at low-oxygen depths were not expected to occur under functional anoxia. Optical oxygen sensors are susceptible to interference from NO, which could result in an overestimate of $[O_2]$ in experiments with especially high rates of NO production (Kraft et al., 2022). Given maximum ammonia oxidation rates of 4.68 ± 0.07 nM N d^{-1}, the release of equivalent amounts of NO would result in an $[O_2]$ overestimate of 0.745 nM during a 24 h incubation, based on the interference curve calculated by Kraft et al. (2022) ($[O_2]$ overestimate $= 0.159 \times [NO]$). Because of this small potential error and the lack of relevant NO measurements, no correction was applied for NO interference.

Optode $[O_2]$ generally agreed with ambient $[O_2]$ measured by the Sea-Bird oxygen sensor attached to the rosette (Fig. S1). Two important exceptions were in the experiments at the base of the ODZ and the deep ODZ core at station PS2, which were not purged before tracer addition. As a result, the ambient $[O_2]$ at these depths was below detection on the Sea-Bird sensor, but the optode $[O_2]$ measurements in the incubation bottles from these depths were 17.7 ± 0.1 and 19.2 ± 0.8 µM, respectively (Fig. S1, Table S1). Additionally, two depths that were suboxic (and thus not sparged prior to tracer addition) had higher optode $[O_2]$ than ambient $[O_2]$: in the deep oxycline at station PS2, ambient $[O_2]$ was 6.8 µM and optode $[O_2]$ was 14.8 ± 0.2 µM; at the oxic–anoxic interface at station PS2, ambient $[O_2]$ was 6.5 µM and optode $[O_2]$ was 9.48 ± 0.09 µM (Fig. S1, Table S1). Because of these few exceptions, we always report both optode and ambient $[O_2]$ in the following figures and text.

2.4 Nitrous oxide isotopocule measurements

Two steps were taken to prepare incubation samples for N_2O isotopocule analysis immediately prior to measurement. Firstly, a 5 mL aliquot was removed from each sample by syringe and replaced with He gas. These aliquots were refrigerated until analysis for $[NO_2^-]$ and $[NH_4^+]$ to check tracer and carrier additions, as mentioned above. After this aliquot was removed, 100 µL of $^{14}NH_4Cl$, $Na^{14}NO_2$, or $K^{14}NO_3$ carrier was added to each sample at final concentrations of 54, 262, or 27 µM, respectively, to bring ^{15}N tracer levels below 5000 ‰. Note that these carrier additions were different from the ^{14}N carrier added to each incubation alongside the ^{15}N tracer; the purpose of the later carrier additions was to pre-

vent exposure of the IRMS system to highly ^{15}N-enriched substrates.

Samples were measured for N_2O concentrations and ^{15}N isotopocules on a custom-built purge and trap system coupled to a Thermo Finnigan DELTA V Plus IRMS, which was run in continuous flow mode and configured to measure m/z 30, 31, 44, 45, and 46 (McIlvin and Casciotti, 2010). These measurements were made under normal operating conditions, using an ionization energy of 124 eV, emission current of 1.50 mA, and accelerating voltage of 3 kV. Samples were analyzed alongside reference materials (B6, S2, and atmosphere-equilibrated seawater) to calibrate the IRMS for scrambling in the ion source with the pyisotopomer software package in Python (Kelly et al., 2023). The number ratios of isotopomers $^{14}N^{15}NO$ and $^{15}N^{14}NO$ were calculated as in Kelly et al. (2023), with the following modifications to account for the contribution of $^{15}N^{15}NO$ to the molecular ion number ratios 46/44 (^{46}R) and 31/30 (^{31}R), which, while negligible at natural abundance, becomes important in tracer experiments.

In natural abundance samples, pyisotopomer solves the following four equations to obtain $^{15}R^{\alpha}$ and $^{15}R^{\beta}$:

$$^{45}R = {}^{15}R^{\alpha} + {}^{15}R^{\beta} + {}^{17}R \tag{1}$$

$$^{46}R = \left({}^{15}R^{\alpha} + {}^{15}R^{\beta}\right){}^{17}R + {}^{18}R + {}^{15}R^{\alpha}{}^{15}R^{\beta} \tag{2}$$

$$^{17}R/{}^{17}R_{\mathrm{VSMOW}} = \left({}^{18}R/{}^{18}R_{\mathrm{VSMOW}}\right)^{\beta}\left[\Delta(^{17}\mathrm{O}) + 1\right] \tag{3}$$

$$^{31}R = \frac{\begin{array}{c}(1-\gamma)\,{}^{15}R^{\alpha} + \kappa\,{}^{15}R^{\beta} + {}^{15}R^{\alpha}{}^{15}R^{\beta} \\ +{}^{17}R\left[1 + \gamma\,{}^{15}R^{\alpha} + (1-\kappa){}^{15}R^{\beta}\right]\end{array}}{1 + \gamma\,{}^{15}R^{\alpha} + (1-\kappa){}^{15}R^{\beta}}, \tag{4}$$

where ^{45}R, ^{46}R, and ^{31}R are the molecular ion number ratios 45/44, 46/44, and 31/30. $^{15}R^{\alpha}$, $^{15}R^{\beta}$, ^{17}R, and ^{18}R denote the number ratios of $^{14}N^{15}N^{16}O$, $^{15}N^{14}N^{16}O$, $^{14}N_2^{17}O$, and $^{14}N_2^{18}O$, respectively, to $^{14}N_2^{16}O$. Here, $\Delta(^{17}O)$ was assumed to be equal to zero. In these equations, the term $(^{15}R^{\alpha})(^{15}R^{\beta})$ represents the statistically expected contribution of $^{15}N^{15}N^{16}O$ to the ^{46}R and^{31}R ion number ratios, based on the probabilities of forming $^{15}N^{15}N^{16}O$. The probability of getting ^{15}N in N^{α} is given by $^{15}R^{\alpha}$, and the probability of getting ^{15}N in N^{β} is given by $^{15}R^{\beta}$; furthermore, the two probabilities are assumed to be independent, so the probability of getting ^{15}N in both positions would be $(^{15}R^{\alpha})(^{15}R^{\beta})$ (Kaiser et al., 2004). Predicting the concentration of $^{15}N^{15}N^{16}O$ from the distribution of ^{15}N in the singly labeled molecules ($^{15}R^{\alpha}$ and $^{15}R^{\beta}$) is a reasonable assumption for natural abundance samples, where the concentration of $^{15}N^{15}N^{16}O$ is extremely low (Kantnerová et al., 2022; Magyar et al., 2016).

For ^{15}N-labeled samples, however, we cannot predict $^{15}N^{15}N^{16}O$ from the singly labeled molecules ($^{15}R^{\alpha}$ and $^{15}R^{\beta}$). This is because the relationship between the formation of $^{15}N^{15}N^{16}O$, $^{14}N^{15}N^{16}O$, and $^{15}N^{14}N^{16}O$ depends on production mechanism and the atom fraction of the substrate. For example, in ^{15}N–NO_2^- experiments with denitrification occurring, there may be far more $^{15}N^{15}N^{16}O$ molecules produced than the amount predicted from the production of $^{14}N^{15}N^{16}O$ and $^{15}N^{14}N^{16}O$. To account for this, we added a term to the equations for ^{46}R and ^{31}R to account for the potential of excess $^{15}N^{15}N^{16}O$ production ($^{15}N^{15}N^{16}O_{\mathrm{excess}}$) in tracer experiments:

$$\begin{aligned}{}^{46}R = {} & \left({}^{15}R^{\alpha} + {}^{15}R^{\beta}\right){}^{17}R + {}^{18}R \\ & + \left({}^{15}R^{\alpha}{}^{15}R^{\beta}\right)_{t0} + {}^{15}N^{15}N^{16}O_{\mathrm{excess}}\end{aligned} \tag{5}$$

$$\begin{aligned}{}^{31}R = {} & (1-\gamma)\,{}^{15}R^{\alpha} + \kappa\,{}^{15}R^{\beta} + \left({}^{15}R^{\alpha}{}^{15}R^{\beta}\right)_{t0} \\ & + {}^{15}N^{15}N^{16}O_{\mathrm{excess}} \\ & + {}^{17}R\left[1 + \gamma\,{}^{15}R^{\alpha} + (1-\kappa){}^{15}R^{\beta}\right] \\ & \overline{\qquad\qquad 1 + \gamma\,{}^{15}R^{\alpha} + (1-\kappa){}^{15}R^{\beta} \qquad\qquad}.\end{aligned} \tag{6}$$

To quantify $^{15}N^{15}N^{16}O_{\mathrm{excess}}$ in tracer samples, we assumed that any increase in ^{46}R over the course of the experiment is due to added $^{15}N^{15}N^{16}O$, i.e., that $\delta(^{18}O)$ remains constant. This should be a reasonable assumption – while denitrification and N_2O consumption could cause natural-abundance-level increases in $\delta(^{18}O)$ and thus ^{46}R (10s of per mil), N_2O production from ^{15}N-labeled substrates are expected to cause much greater increases in ^{46}R (100s to 1000s of per mil). We calculated the term $^{15}N^{15}N^{16}O_{\mathrm{excess}}$ by subtracting the mean ^{46}R at t_0 from the measured ^{46}R at later time points using the pyisotopomer template designed for tracer experiments (Kelly, 2023). Then, we used the "Tracers" function in pyisotopomer, which takes this $^{15}N^{15}N^{16}O_{\mathrm{excess}}$ into account, to calculate $^{15}R^{\alpha}$ and $^{15}R^{\beta}$.

The concentration of $^{44}N_2O$ in each sample was calculated from m/z 44 peak area and from a linear conversion factor divided by the sample volume (McIlvin and Casciotti, 2010). The concentrations of $^{45}N_2O^{\alpha}$, $^{45}N_2O^{\beta}$, and $^{46}N_2O$ were finally calculated by multiplying $^{15}R^{\alpha}$, $^{15}R^{\beta}$, and ^{46}R by the average [$^{44}N_2O$] across all time points for that tracer experiment. Average values of [$^{44}N_2O$] were used to avoid aliasing random variability in [$^{44}N_2O$] over increases in $^{15}R^{\alpha}$, $^{15}R^{\beta}$, and ^{46}R. The analytical precisions for N_2O isotopocule measurements, based on the pooled standard deviations of reference materials run alongside samples, were $\delta(^{15}N^{\alpha}) = 4.4\,‰$, $\delta(^{15}N^{\beta}) = 3.4\,‰$, $\delta(^{15}N^{\mathrm{bulk}}) = 3.5\,‰$, and $\delta(^{18}O) = 2.1\,‰$. The analytical precision was poorer than that in a similar natural abundance dataset (Kelly et al., 2021) due to minor ^{15}N carry-over in some of the standards analyzed immediately following highly enriched samples.

2.5 Nitrite and nitrate isotope measurements

After N_2O analysis, approximately 2 mL of sample remained in each bottle, which was prepared for the analysis of $\delta(^{15}N$–$NO_2^- + NO_3^-)$, $\delta(^{15}N$–$NO_3^-)$, or $\delta(^{15}N$–$NO_2^-)$, to determine the rates of NH_3 oxidation, NO_2^- oxidation, and NO_3^- reduction, depending on the tracer experiment. Samples incubated with ^{15}N–NH_4^+ were prepared for $\delta(^{15}N$–$NO_2^- + NO_3^-)$

analysis using the denitrifier method (Casciotti et al., 2002; Sigman et al., 2001), with updates from McIlvin and Casciotti (2011), to determine rates of NH_3 oxidation. These samples were run on a Thermo Finnigan DELTA^{PLUS} XP IRMS alongside a process blank and reference materials USGS32, USGS34, and USGS35 (Böhlke et al., 2003) to obtain $\delta(^{15}N\text{–}NO_2^- + NO_3^-)$.

Samples incubated with $^{15}N\text{–}NO_2^-$ were first treated with 5 % sulfamic acid (weight by volume, or 10 mM final concentration) to remove $^{15}N\text{–}NO_2^-$ (Granger and Sigman, 2009) then prepared with the denitrifier method for $\delta(^{15}N\text{–}NO_3^-)$ analysis (Casciotti et al., 2002; McIlvin and Casciotti, 2011; Sigman et al., 2001) to determine rates of NO_2^- oxidation. For these analyses, reference materials USGS32, USGS34, and USGS35 (Böhlke et al., 2003) were also treated with 5 % sulfamic acid and prepared with the denitrifier method alongside samples. Incubations with low ambient $[NO_3^-]$ had high $t_0\delta(^{15}N)$ values (> 1000 ‰; Fig. S2). This is likely because NO_3^- is produced when sulfamic acid is added to NO_2^- (Granger and Sigman, 2009), so the sulfamic treatment probably chemically converted some $^{15}N\text{–}NO_2^-$ tracer to $^{15}N\text{–}NO_3^-$; additionally, $^{15}N\text{–}NO_3^-$ is a possible contaminant of the $^{15}N\text{–}NO_2^-$ tracer solutions. Regardless, this would have shifted all three time points equally and thus should not introduce a bias into the slope of $\delta(^{15}N\text{–}NO_3^-)$ with time and the rates calculated from there.

Finally, samples incubated with $^{15}N\text{–}NO_3^-$ were prepared for $\delta(^{15}N\text{–}NO_2^-)$ isotopic analysis with the azide method (McIlvin and Altabet, 2005) to determine rates of NO_3^- reduction to NO_2^-. The 2 mL of remaining sample was transferred into 20 mL vials, where it was prepared alongside reference materials RSIL-N23, -N7373, and -N10219 (Casciotti et al., 2007). Reference materials were diluted from 200 mM working stocks into 3 mL NO_2^--free seawater in 5 and 10 nmol quantities of NO_2^- to correct for the contribution of a consistent blank to a range of sample sizes. The analytical precisions for $\delta(^{15}N\text{–}NO_x^-)$, $\delta(^{15}N\text{–}NO_3^-)$, and $\delta(^{15}N\text{–}NO_2^-)$ were 0.9 ‰, 1.2 ‰, and 0.4 ‰, respectively. The $\delta(^{15}N)$ analytical precision for the denitrifier and azide methods is typically better (McIlvin and Altabet, 2005; Sigman et al., 2001), but tracer measurements tend to have lower analytical precision than natural abundance measurements.

The rates of NH_4^+ and NO_2^- oxidation were calculated using a weighted least-squares linear regression through product ^{15}N vs. incubation time (Fig. S3). Each sample was weighted by its uncertainty, which was calculated based on the slope and intercept of the calibration curve, blank peak area, and sample peak area (Appendix A). Although using this uncertainty calculation is complex, it allows the assessment of relative error and the inclusion of low-peak-area samples that had high enough $\delta(^{15}N)$ enrichments such that the relative error remained below 10 % (and in most cases 1 %). A weighted least-squares regression was used in place of an ordinary least-squares regression to prevent samples with high uncertainties from biasing the slope estimate (e.g., two samples in Fig. S3b). Then, the rate was calculated by

$$\text{rate}\,(\text{nM N d}^{-1}) = \frac{m\left({}^{15}F_{\text{product}}\right)[P]}{{}^{15}F_{\text{substrate}}}, \tag{7}$$

where $m({}^{15}F_{\text{product}})$ is the slope of the atom fraction of ^{15}N in the product vs. incubation time, $[P]$ is the mean product concentration (e.g., NO_3^- in an NO_2^- oxidation experiment), and ${}^{15}F_{\text{substrate}}$ is the atom fraction of ^{15}N in the substrate (e.g., NO_2^- in an NO_2^- oxidation experiment). Our method of estimating individual uncertainties was developed to deal with low NH_3 oxidation rates, which generated low peak areas in $\delta(^{15}N\text{–}NO_3^-)$ samples. Since the rates of NO_3^- reduction were generally much higher than the rates of NH_3 oxidation (Table S2), a parallel method was not needed to estimate individual uncertainties in samples measured with the azide method, i.e., $\delta(^{15}N\text{–}NO_2^-)$ measurements, so rates of NO_3^- reduction were with an ordinary least-squares regression in Eq. (7) instead of a weighted least-squares regression.

2.6 Modeling N_2O production mechanisms

A time-dependent model was constructed to infer the rates and mechanisms of N_2O production from the measured isotopocule time courses in each incubation experiment. While it is possible to calculate rates of hybrid and bacterial N_2O production with linear regressions of $^{45}N_2O$ and $^{46}N_2O$ with time (Trimmer et al., 2016), these calculations cannot take into account ^{15}N transfer between substrates and, more importantly, produce separate rate estimates for separate tracer experiments. They also do not leverage the additional information provided by N_2O isotopomers. We sought to solve for a common set of N_2O production rate constants across the three parallel tracer experiments at a given station and depth, wherein the only differences between each tracer experiment were the starting concentrations of ^{14}N and ^{15}N in NH_4^+, NO_2^-, and NO_3^- (Fig. 2). The model encoded four different N_2O-producing pathways: (1) production solely from NH_4^+, which includes N_2O from hydroxylamine oxidation (referred to as Pathway 1 in Wan et al., 2023b), hybrid production using cellular NO_2^- (referred to as Pathway 2 in Wan et al., 2023b), and nitrifier denitrification using cellular NO_2^-; (2) hybrid production using extracellular NO_2^- (referred to as Pathway 3 in Wan et al., 2023b); (3) production from NO_2^-, i.e., denitrification or nitrifier denitrification using extracellular NO_2^-; and (4) production from NO_3^-, i.e., denitrification using cellular NO_2^- (Fig. 2). Using this model, the relative importance of each of these pathways was determined at each incubation depth based on the production of ^{15}N-labeled N_2O isotopocules in parallel experiments supplied with different ^{15}N substrates.

The concentration of each nitrogen species was modeled as

$$N_{t+1} = N_t + \Delta t\left(\sum_{n=1}^{i} J_n^{\text{source}} - \sum_{n=1}^{k} J_n^{\text{sink}}\right), \tag{8}$$

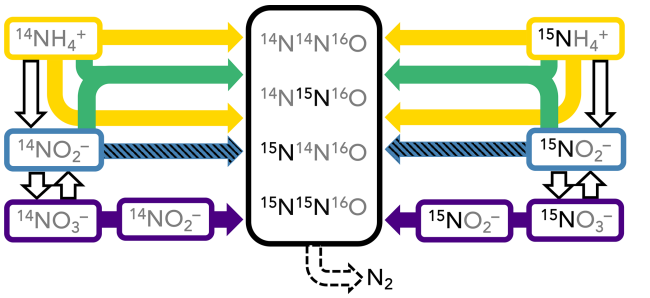

Pathway name	Includes N_2O production from…	Corresponding process in Wan et al. (2023)
Production from solely NH_4^+	Hydroxylamine oxidation	Pathway 1
	Hybrid production using cellular NO_2^-	Pathway 2
	Nitrifier–denitrification using cellular NO_2^-	N/A
Hybrid production	Hybrid production using extracellular NO_2^-	Pathway 3
Production from NO_2^-	Denitrification or nitrifier–denitrification using extracellular NO_2^-	N/A
Production from NO_3^-	Denitrification using cellular NO_2^-	N/A

Figure 2. Schematic of the forward-running model used to solve for rates of N_2O production. Horizontal arrows represent processes whose rates are solved for, while vertical arrows represent processes whose rates are prescribed based on our experimental results. The model solves for second-order rate constants for four N_2O-producing processes: (1) production solely from NH_4^+ (yellow horizontal arrows), which includes N_2O from hydroxylamine oxidation (Wan et al., 2023, Pathway 1), hybrid production using cellular NO_2^- (Wan et al., 2023, Pathway 2), and nitrifier denitrification using cellular NO_2^-; (2) hybrid production using NH_4^+ and extracellular NO_2^- (green arrows; Wan et al., 2023, Pathway 3); (3) production from NO_2^-, i.e., denitrification or nitrifier denitrification using extracellular NO_2^- (hatched blue horizontal arrows); and (4) production from NO_3, i.e., denitrification or nitrifier denitrification using cellular NO_2^- (indigo horizontal arrows). The model also solves for f, the proportion of N^α derived from NO_2^- during hybrid N_2O production. NH_3 oxidation (yellow vertical arrows), NO_2^- oxidation (hatched blue vertical arrows), and NO_3^- reduction to NO_2^- (indigo vertical arrows) are modeled as first-order rates to account for ^{15}N transfer between substrate pools, as described in the main text. Finally, N_2O consumption (dashed black arrow) is modeled as first order to N_2O. It is assumed that, while the distribution of ^{15}N in each tracer experiment at a given station and depth is different, the overall rates and mechanisms of N_2O production are the same regardless of which substrate is labeled. The model is optimized against the observed $^{46}N_2O$, $^{45}N_2O^\alpha$, $^{45}N_2O^\beta$, and $^{44}N_2O$ at each time point in each tracer experiment (black box).

where N_t is the concentration of a given N species (e.g., NH_4^+, NO_2^-, NO_3^-, or N_2O) at time t, N_{t+1} is its concentration at time $t+1$, Δt represents the model time step (days), $\sum_{n=1}^{i} J_n^{\text{source}}$ is the sum of i individual source processes of that species (nM d^{-1}), and $\sum_{n=1}^{k} J_n^{\text{sink}}$ is the sum of k individual sink processes of that species (nM d^{-1}).

The pattern of N_2O isotopocule production for a given process was set by the total rate J of N_2O production for that process multiplied by the probability of forming each isotopocule from a given pair of substrates. The probabilities of forming each isotopocule were based on the atom fractions of the two substrates from which the nitrogen atoms in N_2O are derived:

$$P\left(^{46}N_2O\right) = \left(^{15}F_1\right)\left(^{15}F_2\right) \tag{9}$$

$$P\left(^{45}N_2O^\alpha\right) = f\left(^{15}F_1\right)\left(1-^{15}F_2\right) + (1-f)\left(1-^{15}F_1\right)\left(^{15}F_2\right) \tag{10}$$

$$P\left(^{45}N_2O^\beta\right) = (1-f)\left(^{15}F_1\right)\left(1-^{15}F_2\right) + f\left(1-^{15}F_1\right)\left(^{15}F_2\right) \tag{11}$$

$$P\left(^{44}N_2O\right) = \left(1-^{15}F_1\right)\left(1-^{15}F_2\right), \tag{12}$$

where $P(^{46}N_2O)$, $P(^{45}N_2O^\alpha)$, $P(^{45}N_2O^\beta)$, and $P(^{44}N_2O)$ are the probabilities of forming each isotopocule; $^{15}F_1$ is the atom fraction of ^{15}N in substrate 1; $^{15}F_2$ is the atom fraction of ^{15}N in substrate 2; f is the proportion of N^α derived from substrate 1; and $1-f$ is the proportion of N^α derived from substrate 2. Assuming a 1 : 1 pairing of substrates 1 and 2, f also represents the proportion of N^β derived from substrate 2 and $1-f$ represents the proportion of N^β derived from substrate 1. Processes that derive both nitrogen atoms from the same substrate pool are a special case of Eqs. (9)–(12), where $^{15}F_1 = {}^{15}F_2$. Measuring bulk $^{45}N_2O$ production instead of individual isotopomers (Trimmer et al., 2016) is also a special case of Eqs. (9)–(12), where $P(^{45}N_2O) = P(^{45}N_2O^\alpha) + P(^{45}N_2O^\beta)$ and f cancel out.

To represent each N_2O-producing J term in the model, the rates of N_2O production were modeled as second order:

$$J_i = k_i\,[\text{substrate}_1]\,[\text{substrate}_2], \tag{13}$$

where J_i is the rate of N_2O production process i in nM N d^{-1}, k_i is a second-order rate constant for that process, $[\text{substrate}_1]$ is the concentration of substrate 1 for process i, and $[\text{substrate}_2]$ is the concentration of substrate 2 for process i. Each rate constant k_i was optimized in the model for each station and depth. Again, N_2O production processes that draw both nitrogen atoms from the same substrate are a special case, where $[\text{substrate}_1] = [\text{substrate}_2]$. J was multiplied by 1/2 to convert the rate from nM N d^{-1} to nM N_2O d^{-1}, which was then multiplied by Eqs. (9)–(12) to obtain the rates of production of each isotopocule (note that rates are reported in pM d^{-1}). For example, the rate of hybrid $^{46}N_2O$ production was represented as

$$J_{\text{hybrid}}^{^{46}N_2O} = 1/2\left(k_{\text{hybrid}}\left[NH_4^+\right]\left[NO_2^-\right]\right)\left(^{15}F_{NH_4^+}\right)\left(^{15}F_{NO_2^-}\right), \tag{14}$$

where $J_{\text{hybrid}}^{^{46}N_2O}$ is the rate of $^{46}N_2O$ production via hybrid production in nM N_2O d^{-1}.

To relate the J terms to consumption of the substrate pools (NH_4^+, NO_2^-, and NO_3^-), J draws upon the ^{15}N and ^{14}N substrate pools according to the atom fractions of ^{15}N in each

substrate:

$$J_i^{15} = J_i \cdot {}^{15}F_{\text{substrate}} \text{ and } J_i^{14} = J_i \cdot \left(1 - {}^{15}F_{\text{substrate}}\right), \quad (15)$$

where J_i^{15} and J_i^{14} are the rates of consumption of the ^{15}N and ^{14}N substrate pools by N_2O-producing process i, J_i is the rate in nM N d^{-1} calculated in Eq. (13) for N_2O production process i, and ${}^{15}F_{\text{substrate}}$ is the atom fraction of ^{15}N in the given substrate pool (NH_4^+, NO_2^-, and NO_3^-). Essentially, Eq. (15) relates how each rate J_i draws from the ^{15}N and ^{14}N substrate pools, while Eqs. (9)–(12) determine the ^{15}N and ^{14}N distribution in the product N_2O. For example, the rate of $^{15}NH_4^+$ consumption by hybrid N_2O production was represented as

$$J_{\text{hybrid}}^{^{15}NH_4^+} = \left(k_{\text{hybrid}}\left[NH_4^+\right]\left[NO_2^-\right]\right)\left({}^{15}F_{NH_4^+}\right), \quad (16)$$

where $J_{\text{hybrid}}^{^{15}NH_4^+}$ is the rate of ^{15}N–NH_4^+ consumption via hybrid production in nM N d^{-1}. Equation (16) does not contain the factor of 1/2 in Eq. (14) because the units are nM N d^{-1}, not nM N_2O d^{-1}. Rates of ^{15}N and ^{14}N transfer between substrate pools via NH_3 oxidation, NO_2^- oxidation, and NO_3^- reduction were also included in the model. The model solves for N_2O production rates, given a set of NH_3 oxidation, NO_2^- oxidation, and NO_3^- reduction rates calculated in Sect. 2.5, Eq. (7) (Table S2). These rates were represented in the model as first order:

$$J^{15} = \frac{k}{\alpha}\left[{}^{15}N\right] \text{ and } J^{14} = k\left[{}^{15}N\right], \quad (17)$$

where J^{15} and J^{14} represent the rates of ^{15}N and ^{14}N transformation via NH_3 oxidation, NO_2^- oxidation, or NO_3^- reduction; k is a first-order rate constant derived from measured rates; α is a fractionation factor (Table S3); [^{15}N] is the concentration of the ^{15}N species; and [^{14}N] is the concentration of the ^{14}N species. N_2O consumption was modeled as first order to the concentration of each isotopocule, based on the [O_2]-corrected rates of N_2O consumption measured on the same cruise (Sun et al., 2021a).

The model was optimized against isotopocule data at each time step in each tracer experiment (Fig. S4). The parameters being optimized (inputs to the cost function) were the second-order rate constants k_i for N_2O production solely from NH_4^+, N_2O production from NO_2^- via denitrification or nitrifier denitrification, N_2O production from NO_3^- via denitrification, hybrid N_2O production using extracellular NO_2^-, and f (Fig. 2). In the model, these are all separate processes that operate independently. The model was optimized using the Nelder–Mead simplex algorithm (Nelder and Mead, 1965), implemented in the SciPy optimization library (Virtanen et al., 2020), which has been used successfully for natural abundance N_2O isotopocule models (Monreal et al., 2022). Model error was estimated by optimizing the model at each station and depth with 100 combinations of model parameters, randomly varying the initial concentrations of each ^{15}N and ^{14}N substrate and rate constants for NH_3 oxidation, NO_2^- oxidation, and NO_3^- oxidation by up to 25 %.

To ground-truth the model, rates of N_2O production obtained from the model were compared to the measured net rates of $^{46}N_2O$ production (Fig. S5). For processes drawing both nitrogen atoms from the same substrate pool (i.e., not hybrid production), the modeled rates of N_2O production from each substrate should correspond roughly to the net rate of $^{46}N_2O$ production from the same ^{15}N-labeled substrate. Higher modeled rates of N_2O production solely from NH_4^+ generally corresponded to higher net rates of $^{46}N_2O$ production from ^{15}N–NH_4^+ (Fig. S5a). Since the model cannot produce negative rates, negative net rates of $^{46}N_2O$ production from ^{15}N–NH_4^+ corresponded to modeled N_2O production rates equal to zero (Fig. S5a). Modeled rates of N_2O production from NO_2^- and NO_3^- via denitrification also corresponded to higher measured rates of $^{46}N_2O$ production from ^{15}N–NO_2^- and ^{15}N–NO_3^-, respectively (Fig. S5b, c).

3 Results

3.1 Depth distributions of oxygen, nitrite, and nitrous oxide

Station PS1, which was at the edge of the ODZ, represented a "background" station with no secondary NO_2^- maximum and a less-pronounced minimum in [N_2O] below the oxycline (Fig. S6; Kelly et al., 2021). At station PS1, the oxic–anoxic interface, defined in this study as the depth just above the ODZ, occurred at the base of the mixed layer at 100 m depth (Fig. S6). Station PS2 was near the geographic center of the oxygen-deficient region and had a secondary NO_2^- maximum of 2.2 µM, indicating functional anoxia (Fig. S6). The oxic–anoxic interface at station PS2 occurred at 92 m depth (Fig. S6). Below the oxic–anoxic interface, [N_2O] declined to 4.5 ± 0.3 nM before increasing again at the base of the secondary NO_2^- maximum and reaching a local maximum around 800 m depth. Station PS3 was approximately 19 km from the coast of Mexico and had a shallow oxic–anoxic interface that moved up and down on timescales of days: on 10 April, the oxic–anoxic interface occurred at 40 m depth; 2 d later, the oxic–anoxic interface had deepened to 62 m depth. Experiments were performed at the oxic–anoxic interface on both days and are designated with the abbreviations "Interface" and "Interface2" in the experimental metadata (Table S1). The chemical profiles from 11 April (Fig. S6), on which the near-surface [N_2O] maximum occurred at 61 m (Kelly et al., 2021), are displayed along with the rate data in this study. Station PS3 had a pronounced secondary NO_2^- maximum of 2.8 µM at 161 m depth (Fig. S6) and an NH_4^+ maximum of 400 nM at 15 m depth (not shown). On 11 April, [N_2O] reached a maximum of 195 ± 13 nM at the oxic–anoxic interface and declined below this depth. Below 600 m depth, [N_2O] began to increase again to 44 ± 3 nM. At ev-

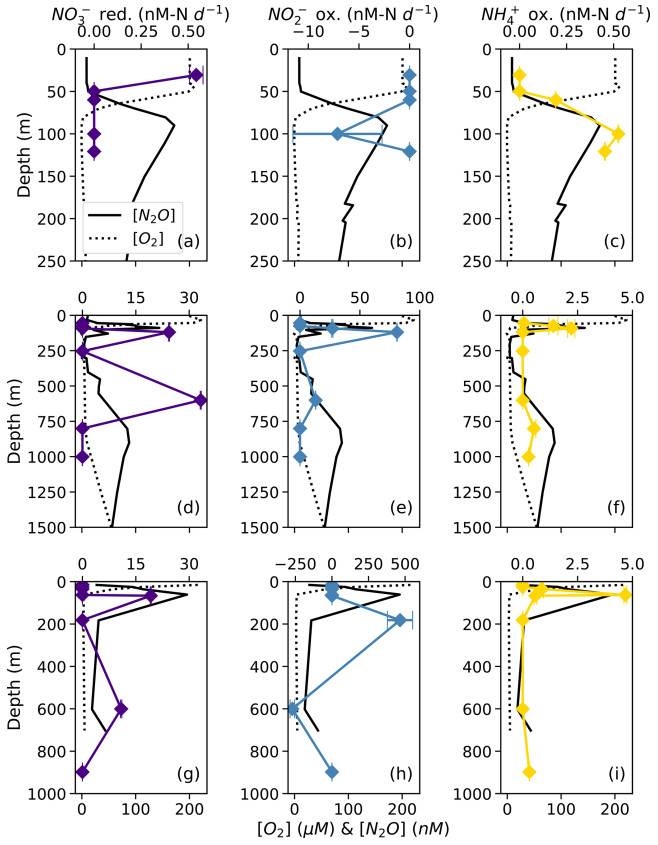

Figure 3. Rates of NO_3^- reduction to NO_2^- (**a**, **d**, **g**; indigo), NO_2^- oxidation to NO_3^- (**b**, **e**, **h**; blue), and NH_3 oxidation to $NO_2^- + NO_3^-$ (**c**, **f**, **i**; yellow) at stations PS1 **(a–c)**, PS2 **(d–f)**, and PS3 **(g–i)**. Rates are plotted over depth profiles of dissolved $[O_2]$ (dashed lines) and $[N_2O]$ (solid lines; from Kelly et al., 2021). Error bars represent rate error, calculated from the error of the slope of product ^{15}N vs. time. Note the different x-axis scales for rate measurements (top x axes) and $[O_2]$ and $[N_2O]$ (bottom x axes).

ery station, a deep secondary chlorophyll *a* maximum was observed near the oxic–anoxic interface, where photosynthetically active radiation was much reduced and $[NO_3^-]$ was abundant (Travis et al., 2023). This secondary chlorophyll *a* maximum tended to develop between the depths of the oxic–anoxic interface and the secondary NO_2^- maximum (Travis et al., 2023).

3.2 Nitrification and nitrate reduction rates

NO_3^- reduction to NO_2^- occurred at rates ranging from 0.54 ± 0.04 to 33.2 ± 0.1 nM N d^{-1} (Table S2). There was a small, significant rate of NO_3^- reduction to NO_2^- in apparently aerobic waters near the surface at station PS1 (Fig. 3a). The highest rates of NO_3^- reduction to NO_2^- occurred in the deep, anoxic waters at station PS2 (33.24 ± 0.01 nM N d^{-1}; Fig. 3d) and in the secondary chlorophyll maximum at station PS3 (19.2 ± 0.1 nM N d^{-1}; Fig. 3g).

NO_2^- oxidation rates ranged from 13.05 ± 0.08 to 465 ± 86 nM N d^{-1} (Table S2). The highest rates of NO_2^- oxidation occurred within apparently oxygen-deficient waters at 81.0 ± 0.2 nM N d^{-1} in the secondary chlorophyll *a* maximum at station PS2 and at 465 ± 86 nM N d^{-1} in the secondary NO_2^- maximum at station PS3 (Fig. 3e, h; Table S2). Note that these are potential rates, since the ^{15}N addition was generally much greater than the ambient concentration (Lipschultz, 2008). In some cases, NO_2^- oxidation rates appeared negative due to a decrease in ^{15}N–NO_3^- vs. incubation time (Fig. 3b, h), which was likely an artifact of the elevated t_0 $\delta(^{15}N)$ values in some of our ^{15}N–NO_2^- treatments (discussed above). We chose, however, not to left-censor the data.

NH_3 oxidation to NO_2^- occurred at small but significant rates ranging from 0.19 ± 0.0004 to 4.68 ± 0.07 nM N d^{-1} (Table S2). At every station, rates of NH_3 oxidation peaked near the base of the mixed layer at the same depth as the near-surface $[N_2O]$ maximum (Fig. 3c, f, i). At station PS2, NH_3 oxidation showed a secondary peak at the same depth as the deep $[N_2O]$ maximum (Fig. 3f). At station PS3, there was also a small, significant rate of NH_3 oxidation (0.303 ± 0.005 nM N d^{-1}) at 898 m, which was close to the bottom depth (Fig. 3i). Rates of NH_3 oxidation were generally lower than NO_2^- oxidation and undetectable in oxygen-deficient waters (Fig. 3c, f, i).

3.3 Net production rates of $^{45}N_2O^{\alpha}$, $^{45}N_2O^{\beta}$, and $^{46}N_2O$ (measured net rates)

At each station, the observed rates of net $^{46}N_2O$ (Fig. 4), $^{45}N_2O^{\alpha}$, and $^{45}N_2O^{\beta}$ (Fig. 5) production from ^{15}N–NH_4^+, ^{15}N–NO_2^-, and ^{15}N–NO_3^- all peaked at or just below the oxic–anoxic interface, where the near-surface $[N_2O]$ maximum was found. There were also relatively higher rates of net $^{46}N_2O$ production from ^{15}N–NO_2^- and ^{15}N–NO_3^- within the secondary NO_2^- maximum (253 m) at station PS2 (Fig. 4d–e). Relatively high rates of net $^{45}N_2O^{\alpha}$ and $^{45}N_2O^{\beta}$ production also occurred in the secondary NO_2^- maximum at stations PS2 (253 m; Fig. 5d–e) and PS3 (182 m; Fig. 5g–h). The net rates of $^{45}N_2O^{\alpha}$ and $^{45}N_2O^{\beta}$ production varied in concert at almost every station and depth, with a few exceptions (Fig. 5).

For example, in the secondary NO_2^- maximum (182 m) at station PS3, in the ^{15}N–NO_2^- experiment, the production of $^{45}N_2O^{\alpha}$ was 60 ± 30 pM N_2O d^{-1} ($p = 0.09$) and there was no significant production of $^{45}N_2O^{\beta}$ (Fig. 5h). In the parallel ^{15}N–NH_4^+ experiment, the production of $^{45}N_2O^{\beta}$ was 0.7 ± 0.3 pM N_2O d^{-1} ($p = 0.06$) and there was no significant production of $^{45}N_2O^{\alpha}$. At this station and depth, f (the proportion of N^{α} derived from NO_2^-) was equal to 0.9 ± 0.2 (Table S4). The second experiment in which labeling was unequal occurred at the oxic–anoxic interface (92 m) at station PS2, where, in the ^{15}N–NH_4^+ experiment, the production of $^{45}N_2O^{\alpha}$ was 5 ± 2 pM N_2O d^{-1} ($p = 0.02$) and there was

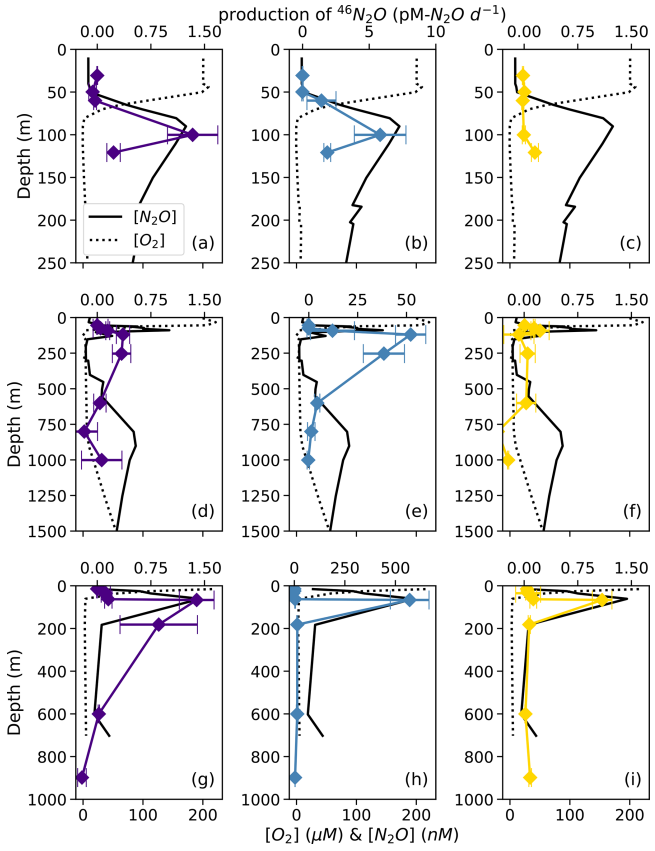

Figure 4. Net $^{46}N_2O$ production from ^{15}N–NO_3^- (**a**, **d**, **g**; indigo), ^{15}N–NO_2^- (**b**, **e**, **h**; blue), and ^{15}N–NH_4^+ (**c**, **f**, **i**; yellow) at stations PS1 **(a–c)**, PS2 **(d–f)**, and PS3 **(g–i)**. N_2O production rates are plotted over depth profiles of dissolved $[O_2]$ (dashed lines) and $[N_2O]$ (solid lines; from Kelly et al., 2021). Error bars are calculated from the linear regression slope error of $^{46}N_2O$ vs. incubation time. Note the different x-axis scales for $^{46}N_2O$ production (top x axes) and $[O_2]$ and $[N_2O]$ (bottom x axes) .

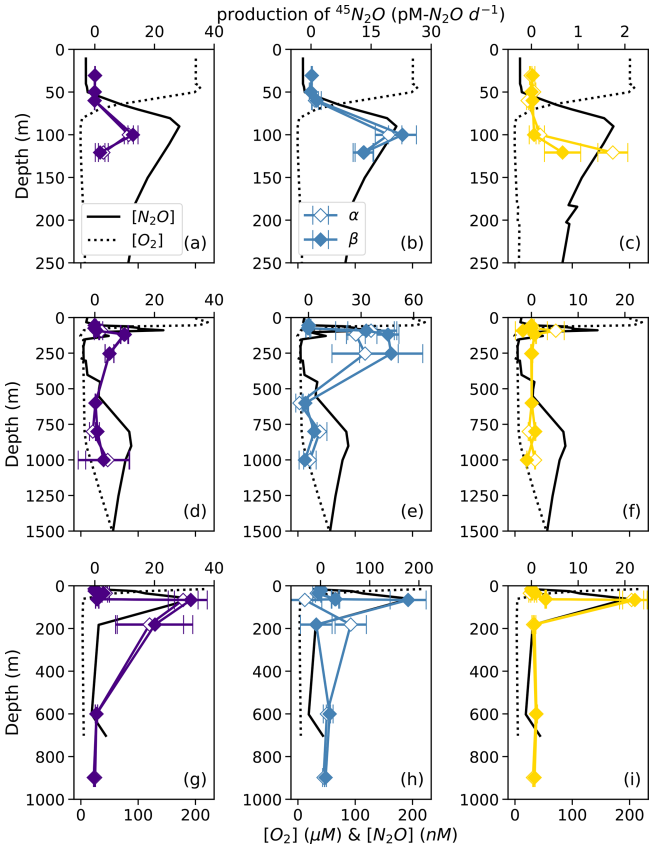

Figure 5. Net $^{45}N_2O^{\alpha}$ (open symbols) and $^{45}N_2O^{\beta}$ (closed symbols) production from ^{15}N–NO_3^- (**a**, **d**, **g**; indigo), ^{15}N–NO_2^- (**b**, **e**, **h**; blue), and ^{15}N–NH_4^+ (**c**, **f**, **i**; yellow) at stations PS1 **(a–c)**, PS2 **(d–f)**, and PS3 **(g–i)**. N_2O production rates are plotted over depth profiles of dissolved $[O_2]$ (dashed lines) and $[N_2O]$ (solid lines; from Kelly et al., 2021). Error bars are calculated from the linear regression slope error of $^{45}N_2O$ vs. incubation time. Note the different x-axis scales for $^{45}N_2O$ production (top x axes) and $[O_2]$ and $[N_2O]$ (bottom x axes) .

no significant production of $^{45}N_2O^{\beta}$ (Fig. 5f). Here, f was equal to 0.2 ± 0.1. Finally, at the mid-oxycline depth (25 m) at station PS3, in the ^{15}N–NH_4^+ experiment, the production of $^{45}N_2O^{\alpha}$ was 0.23 ± 0.8 pM N_2O d^{-1} ($p = 0.02$) and there was no significant production of $^{45}N_2O^{\beta}$. Here, f was statistically indistinguishable from zero.

At many stations and depths, the net production of $^{45}N_2O^{\alpha}$ and $^{45}N_2O^{\beta}$ exceeded the values expected from $^{46}N_2O$ production for a process that draws both nitrogen atoms from the same substrate pool (Fig. S7). This expected value is calculated from the atom fraction of ^{15}N in the substrate and from a binomial distribution of the isotopocules of N_2O during N_2O production (Trimmer et al., 2016):

$$p^{45}_{\text{expected}} = \frac{p^{46}}{\left({}^{15}F\right)^2} 2\left({}^{15}F\right)\left(1-{}^{15}F\right) = \frac{p^{46}}{{}^{15}F} 2\left(1-{}^{15}F\right), \quad (18)$$

where p^{45}_{expected} is the expected production of $^{45}N_2O^{\alpha}$ and $^{45}N_2O^{\beta}$ from a process that draws both nitrogen atoms from the same substrate pool, p^{46} is the net production rate of $^{46}N_2O$, and ^{15}F is the atom fraction of ^{15}N in the substrate pool (for example, NO_2^- in a ^{15}N–NO_2^- experiment). Then, excess production of $^{45}N_2O$ is any $^{45}N_2O$ production above and beyond this expected rate:

$$p^{45}_{\text{excess}} = p^{45} - p^{45}_{\text{expected}} = p^{45} - \frac{p^{46}}{{}^{15}F} 2\left(1-{}^{15}F\right), \quad (19)$$

where p^{45}_{excess} is the excess production of $^{45}N_2O$ above and beyond that expected for a process drawing both nitrogen atoms from the same pool and p^{45} is the measured net production of $^{45}N_2O$. The equations for $^{45}N_2O^{\alpha}$ and $^{45}N_2O^{\beta}$ are the same as Eq. (19), except for a factor of 2. In many of the ^{15}N–NH_4^+ experiments, there was significant excess $^{45}N_2O^{\alpha}$ and $^{45}N_2O^{\beta}$ production (Fig. S7a). Similarly, there was sig-

nificant excess $^{45}N_2O^{\alpha}$ and $^{45}N_2O^{\beta}$ production in many of the ^{15}N–NO_2^- experiments, although this was harder to discern due to the wider range of atom fractions in these experiments (Fig. S7b). In a few experiments, excess $^{45}N_2O^{\alpha}$ and $^{45}N_2O^{\beta}$ production diverged.

3.4 N_2O production mechanisms and yields (model results)

Based on model results, the rates of N_2O production from NO_3^- (denitrification using cellular NO_2^-; Fig. 2) were the highest among the N_2O production processes measured in this study. At suboxic to anoxic depths, the rates of N_2O production from NO_3^- were orders of magnitude higher than all the other N_2O production rates (Fig. 6). N_2O production from NO_3^- reached its maximum value (1600 ± 400 pM $N_2O\,d^{-1}$; Table S4) at the depth of the near-surface [N_2O] maximum at every station (Fig. 6a, e, i), where there were also high rates of NO_3^- reduction to NO_2^- at stations PS2 and PS3 (Fig. 6e, i). N_2O production from NO_2^- (denitrification using extracellular NO_2^-; Fig. 2) exhibited lower rates, with a maximum of 510 ± 30 pM $N_2O\,d^{-1}$ (Table S4). At stations PS1 and PS3, N_2O production from NO_2^- peaked at the depth of the near-surface [N_2O] maximum (Fig. 6b, j); at station PS2, N_2O production from NO_2^- was observed in the near-surface [N_2O] maximum but peaked in the secondary NO_2^- maximum (253 m; Fig. 6f).

Hybrid N_2O production occurred at a similar rate to N_2O production from NO_2^-, ranging from 0.061 ± 0.005 to 230 ± 80 pM $N_2O\,d^{-1}$. Hybrid N_2O production peaked within the near-surface [N_2O] maximum at all stations (Fig. 6c, g, k). At station PS2, hybrid N_2O production exhibited the highest rates at the same depths as NH_3 oxidation, with a secondary peak in the deep [N_2O] maximum (Fig. 6g). At station PS3, hybrid N_2O production, like NH_3 oxidation, exhibited a small, significant rate at 898 m, which was very close to the bottom depth at station PS3 (Table S4).

N_2O production solely from NH_4^+ occurred at the smallest rates overall, ranging from 0.010 ± 0.004 to 8 ± 2 pM $N_2O\,d^{-1}$ (Table S4). N_2O production solely from NH_4^+ peaked around the near-surface [N_2O] maximum at each station (Fig. 6d, h, l) and in the secondary NO_2^- maximum at station PS2 (Fig. 6h).

The percentage of N_2O production from NH_4^+ comprised of hybrid N_2O was calculated as

$$\%\,\text{hybrid} = \frac{\text{hybrid } N_2O\left(\text{nM } N_2O\,d^{-1}\right)}{\begin{array}{c}N_2O \text{ from hydroxylamine } \left(\text{nM } N_2O\,d^{-1}\right) \\ +\text{hybrid } N_2O\ \left(\text{nM } N_2O\,d^{-1}\right)\end{array}}. \quad (20)$$

On average, hybrid N_2O production was 86 ± 28 % of N_2O production from NH_4^+. Hybrid N_2O production was > 75 % of the total N_2O production from NH_4^+ at all stations and depths except for the top of the oxycline at station PS1 (Fig. 7a), the middle of the oxycline at station PS2 (Fig. 7b), and the top of the oxycline at station PS3 (Fig. 7c), where it comprised 0 %, 68 %, and 19 % of N_2O production from NH_4^+, respectively. Hybrid production as a percentage of total N_2O production from NH_4^+ declined with increasing dissolved oxygen (Fig. S8), although more measurements are needed to fully evaluate this trend.

The percentage of hybrid N_2O production as a proportion of total N_2O production was more variable and tended to decline with decreasing dissolved oxygen as production from NO_3^- increased (Fig. 7). Hybrid N_2O production was greater than 75 % of total N_2O production only at the surface at station PS1 (Fig. 7a), at the top of the oxycline and in the deep [N_2O] maximum at station PS2 (Fig. 7b), and in the deep [N_2O] maximum at station PS3 (Fig. 7c).

N_2O production from NO_3^- comprised a much greater proportion of total N_2O production overall (Fig. 7). In the near-surface [N_2O] maximum at station PS1, N_2O production was predominantly (95.4 %) from NO_3^-, with smaller contributions from hybrid production (4.0 %) and denitrification from NO_2^- (0.6 %; Fig. 7a). In the near-surface [N_2O] maximum at station PS2, N_2O production was 60.2 % from NO_3^-, 32.1 % from hybrid production, 7.3 % from NO_2^-, and 0.4 % solely from NH_4^+ (Fig. 7b). In the near-surface [N_2O] maximum at station PS3, N_2O production was 87.0 % from NO_3^-, 12.4 % from hybrid production, 0.5 % from NO_2^-, and 0.1 % solely from NH_4^+ (Fig. 7c).

3.5 Oxygen dependence of N_2O production

The oxygen dependencies of N_2O production pathways were determined by fitting model-derived N_2O production pathways vs. [O_2] using the following rate law:

$$\text{rate} = ae^{-b[O_2]}. \quad (21)$$

In this analysis, both ambient [O_2] measured by the Sea-Bird sensor mounted on the rosette ("ambient [O_2]") and [O_2] measured by chemiluminescent optodes mounted inside incubation bottles ("incubation [O_2]") were examined. The rate dependencies on ambient and incubation [O_2] reflect both preconditioning (i.e., the ambient [O_2] in which the microbial community was living before the incubation experiment) and the response to perturbation (i.e., the experimental conditions inside the incubation bottles, if different from the environment). Those incubations that had higher incubation [O_2] than the ambient [O_2] had received small oxygen perturbations.

N_2O production via denitrification exhibited an exponentially declining relationship with dissolved O_2, where N_2O production from NO_2^- was more inhibited by dissolved O_2 than N_2O production from NO_3^- was (Fig. 8). When looking at the oxygen dependence of denitrification, we found several instances of N_2O production from NO_3^- via denitrification with dissolved [O_2] greater than 3 µM (Fig. 8a–b). For example, at the oxic–anoxic interface at station PS2, where ambient [O_2] was 6.49 µM and incubation [O_2] was 6.29 ± 0.07 µM (Table S1), N_2O production from NO_3^- was

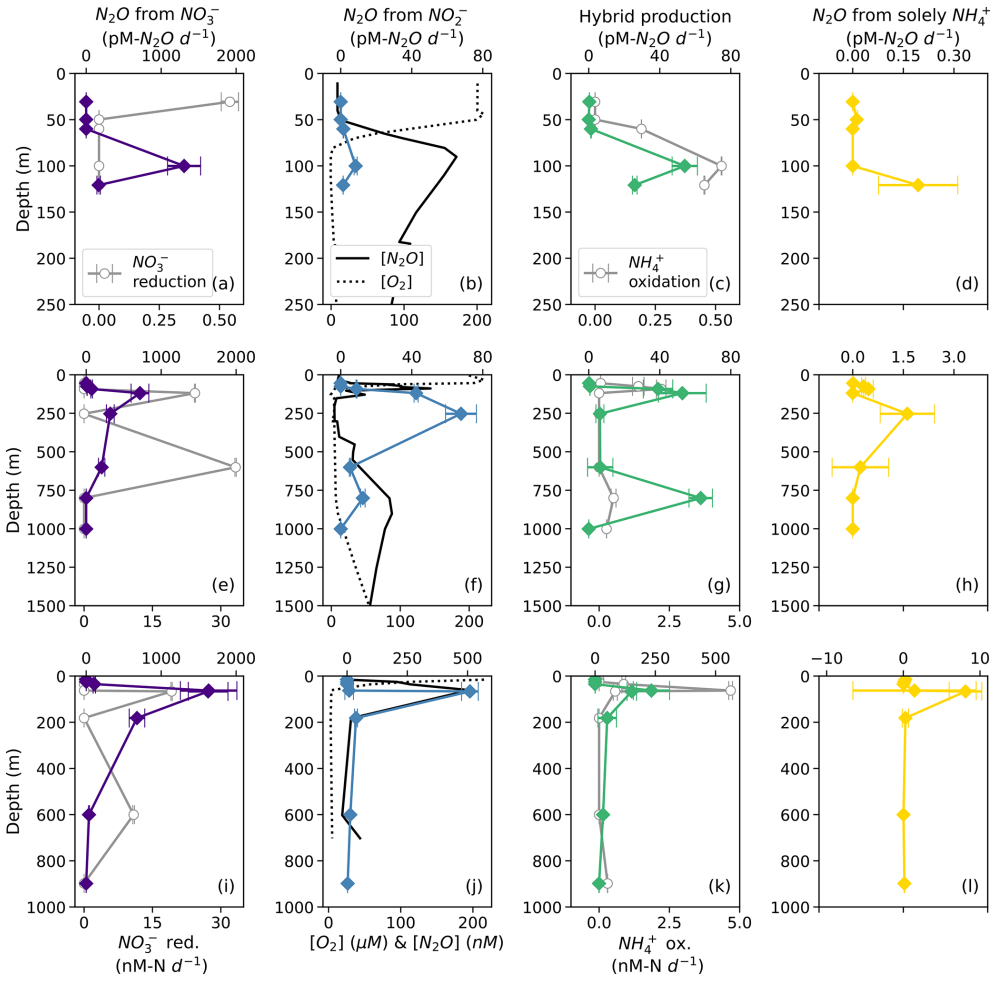

Figure 6. N_2O production from NO_3^- (**a**, **e**, **i**; indigo diamonds), N_2O production from NO_2^- (**b**, **f**, **j**; blue diamonds), hybrid N_2O production (**c**, **g**, **k**; green diamonds), and N_2O production solely from NH_4^+ (**d**, **h**, **l**; yellow diamonds) at stations PS1 **(a–d)**, PS2 **(e–h)**, and PS3 **(i–l)**. Panels **(a)**, **(e)**, and **(i)** also show rates of NO_3^- reduction to NO_2^- (open circles). Panels **(b)**, **(f)**, and **(j)** show depth profiles of dissolved [O_2] (dashed lines) and [N_2O] (solid lines; from Kelly et al., 2021). Panels **(c)**, **(g)**, and **(k)** show rates of NH_3 oxidation (gray circles). N_2O production rate error bars are calculated from 100 model optimizations, varying key parameters by up to 25 %. Note the different x-axis scales for NO_3^- reduction to NO_2^- (**a**, **e**, **i**; bottom), N_2O production (top), [O_2] and [N_2O] (**b**, **f**, **j**; bottom), and NH_3 oxidation (**c**, **g**, **k**; bottom).

70 ± 10 pM $N_2O\,d^{-1}$ (Fig. 6e, Table S4). N_2O production from NO_2^- at the same station and depth was 8.9 ± 0.2 pM $N_2O\,d^{-1}$ (Fig. 6f, Table S4). Similarly, at the oxic–anoxic interface of station PS3, where ambient [O_2] was 12.48 µM and incubation [O_2] was 6.64 ± 0.03 µM (Table S1), N_2O production from NO_3^- was 120 ± 20 pM $N_2O\,d^{-1}$ (Fig. 6i, Table S4). There were also two anoxic depths at station PS2 that were not sparged with He before tracer addition ("base of ODZ" and "deep ODZ core"), where ambient [O_2] was below detection but incubation [O_2] was significantly elevated (17.7 ± 0.1 and 19.2 ± 0.8 µM, respectively; Table S1). At these depths, N_2O production from NO_2^- was 12 ± 1 and 5.2 ± 0.4 pM $N_2O\,d^{-1}$, respectively (Fig. 6f, Table S4). N_2O production from NO_3^- at the "deep ODZ core" depth was 210 ± 40 pM $N_2O\,d^{-1}$ (Table S4).

Hybrid N_2O production rates also decreased exponentially with increasing dissolved [O_2] (Fig. 9a–b). Fitting hybrid rates vs. ambient [O_2] produced a rate (Eq. 21) with $a = 65.83$ and $b = 0.17$ (Fig. 9a); hybrid rates vs. incubation [O_2] produced fits with $a = 76.26$ and $b = 0.067$ (Fig. 9b).

The rate of N_2O production solely from NH_4^+ also decreased exponentially with increasing dissolved [O_2]. The highest rates of N_2O production solely from NH_4^+ occurred in the secondary chlorophyll maximum at station PS3 (Table S4), where dissolved oxygen was below detection. N_2O yield during production solely from NH_4^+ also exhibited exponentially decreasing relationships with dissolved [O_2] (Fig. 9e–f). To ensure mass balance in terms of NH_4^+ consumption (Fig. S9), N_2O yield (%) during production solely

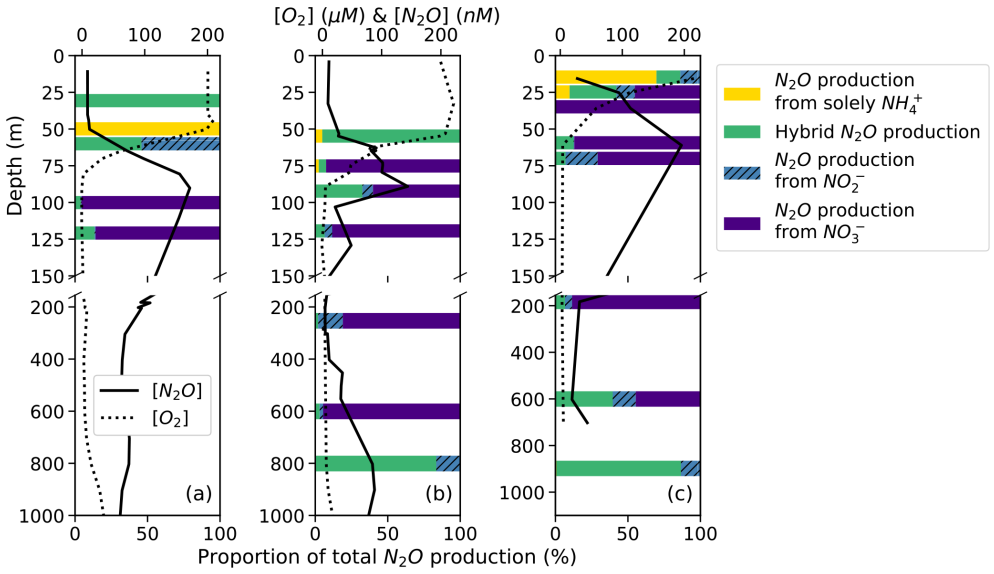

Figure 7. N_2O production solely from NH_4^+ (yellow bars), hybrid N_2O production (green bars), N_2O production from NO_2^- (hatched blue bars), and N_2O production from NO_3^- (indigo bars) as proportions of total N_2O production at stations PS1 **(a)**, PS2 **(b)**, and PS3 **(c)**. Data are plotted over depth profiles of dissolved $[O_2]$ (dashed lines) and $[N_2O]$ (solid lines; from Kelly et al., 2021). Note broken y axes and different x-axis scales for $[O_2]$ and $[N_2O]$ (top) and for proportions (bottom).

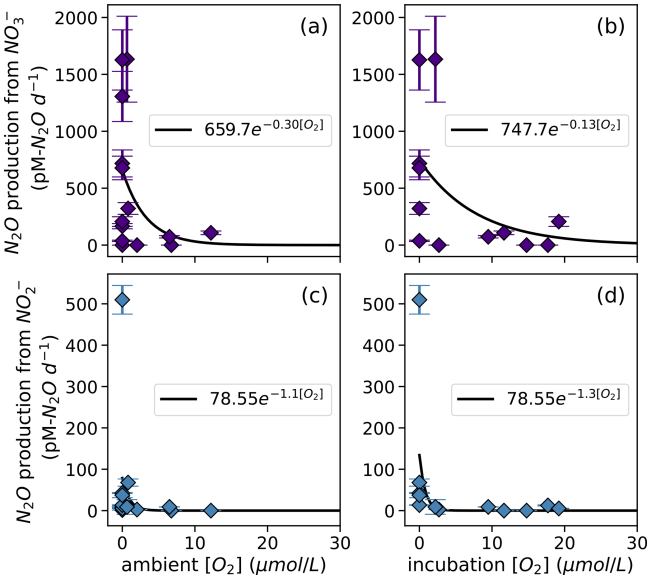

Figure 8. N_2O production from NO_3^- via denitrification **(a, b)** and from NO_2^- via denitrification **(c, d)**, measured at a range of $[O_2]$ measured by a Seabird sensor **(a, c)** or by chemiluminescent optodes mounted inside incubation bottles **(b, d)**. Curves of form, yield $= ae^{-O_2 b}$, are fit through the data (black lines); values of a and b are shown in white boxes in each plot.

from NH_4^+ was calculated as

$$\text{yield}\,(\%) = \frac{2\left[\text{N}_2\text{O solely from NH}_4^+\ \left(\text{nM N}_2\text{O d}^{-1}\right)\right]}{\begin{array}{c}2\left[\text{N}_2\text{O solely from NH}_4^+\ \left(\text{nM N}_2\text{O d}^{-1}\right)\right] \\ +\text{hybrid N}_2\text{O}\ \left(\text{nM N}_2\text{O d}^{-1}\right) \\ +\text{NH}_3\ \text{oxidation}\ \left(\text{nM N d}^{-1}\right)\end{array}}, \quad (22)$$

where N_2O production solely from NH_4^+ is in units of nM $N_2O\,d^{-1}$, hybrid N_2O production is in units of nM $N_2O\,d^{-1}$, and NH_3 oxidation to NO_2^- is in units of nM $N\,d^{-1}$. This assumes that the formation of N_2O solely from NH_4^+ draws two nitrogen atoms from the NH_4^+ pool, while hybrid N_2O production and the oxidation of NH_4^+ to NO_2^- each draw one atom from the NH_4^+ pool (Fig. S9). Following the same convention, N_2O yield (%) during hybrid production was calculated as

$$\text{yield}\,(\%) = \frac{\text{hybrid N}_2\text{O}\ \left(\text{nM N}_2\text{O d}^{-1}\right)}{\begin{array}{c}2\left[\text{N}_2\text{O solely from NH}_4^+\ \left(\text{nM N}_2\text{O d}^{-1}\right)\right] \\ +\text{hybrid N}_2\text{O}\ \left(\text{nM N}_2\text{O d}^{-1}\right) \\ +\text{NH}_3\ \text{oxidation}\ \left(\text{nM N d}^{-1}\right)\end{array}}. \quad (23)$$

The maximum N_2O yield from hybrid production was 21 ± 7 % (Fig. 9c, d). while the maximum N_2O yield during production solely from NH_4^+ was 2.2 ± 0.7 % (Fig. 9e, f). The N_2O yield during production solely from NH_4^+ declined more sharply with increased O_2 than the N_2O yield during hybrid production did (Fig. 9c–f).

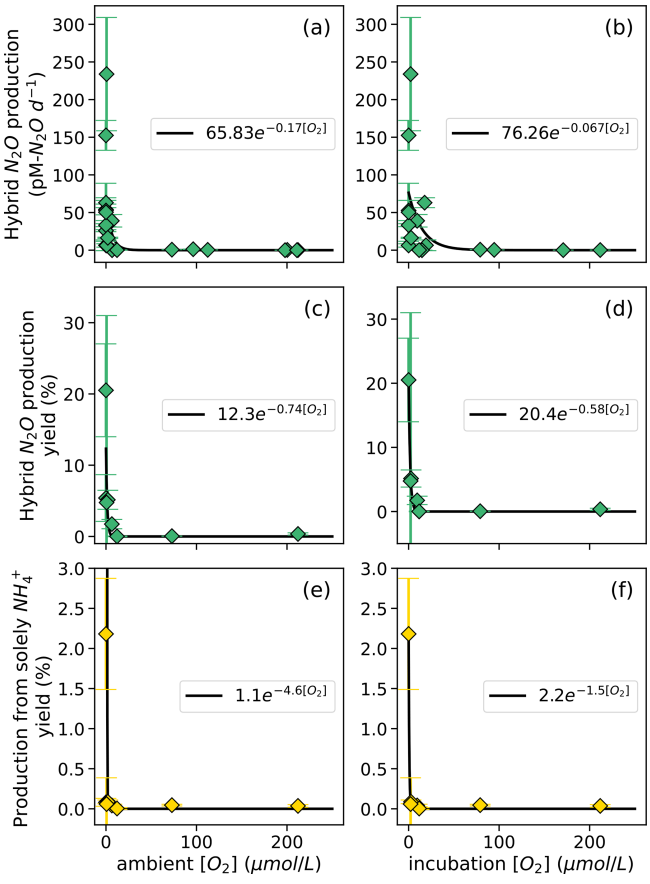

Figure 9. Hybrid N_2O production rates **(a, b)**, N_2O yield (%) during hybrid production **(c, d)**, and N_2O yield (%) during production solely from NH_4^+ **(e, f)** along a range of ambient $[O_2]$ measured by a Seabird sensor for the Niskin bottles from which samples were taken **(a, c, e)** and of $[O_2]$ measured by chemiluminescent optodes mounted inside incubation bottles **(b, d, f)**. Error bars are calculated from 100 model optimizations, varying key parameters by up to 25 %. Yields are only calculated at stations and depths where rates of NH_3 oxidation are greater than 0. Curves of form, rate $= ae^{-b[O_2]}$, are fit through the data (black lines); values of a and b are shown in white boxes in each plot.

4 Discussion

In this study, we found that N_2O production from denitrification was the dominant source of N_2O both within the ODZ and in the upper oxycline. Hybrid N_2O production was a smaller but significant contributor to N_2O in the upper oxycline, and the primary source of N_2O in the deep oxycline. N_2O production solely from NH_4^+ (which includes N_2O from hydroxylamine oxidation, hybrid production with cellular NO_2^-, and nitrifier denitrification with cellular NO_2^-) was negligible everywhere except surface waters. Our findings of equal formation of $^{45}N_2O^{\alpha}$ and $^{45}N_2O^{\beta}$ in most experiments indicate that N^{α} retains an equal proportion of NO_2^- and NH_4^+-derived N during hybrid production, which may imply that hybrid N_2O production exhibits a constant $\delta(^{15}N^{sp})$. All of the processes measured in this study exhibited a strong dependence on dissolved oxygen, although denitrification was less inhibited by dissolved oxygen than previous work would suggest.

4.1 Rates of N_2O production via denitrification

Based on our rate data, N_2O production from NO_3^- is the dominant source of N_2O in both the near-surface $[N_2O]$ maximum and the anoxic ODZ core. This agrees well with natural abundance isotopocule measurements in the ETNP, which indicate that the near-surface $[N_2O]$ maximum is likely to comprise $\sim 80\,\%$ N_2O produced via denitrification and $\sim 20\,\%$ N_2O produced via nitrification or archaeal N_2O production, producing a local minimum in $\delta(^{15}N^{sp})$ (Kelly et al., 2021). Natural abundance isotopomer work has shown that N_2O production from NO_3^- could be an important source of N_2O in the anoxic core of ODZs, as long as it has a positive $\delta(^{15}N^{sp})$ (Casciotti et al., 2018; Kelly et al., 2021; Monreal et al., 2022). While denitrification is generally accepted to produce N_2O with $\delta(^{15}N^{sp}) \approx 0\,‰$ (Sutka et al., 2006; other refs), some strains of denitrifying bacteria can produce N_2O with $\delta(^{15}N^{sp}) = 10\,‰$–$22\,‰$ (Toyoda et al., 2005; Wang et al., 2023) and denitrifying fungi produce N_2O with $\delta(^{15}N^{sp}) = 35\,‰$–$37\,‰$ (Lazo-Murphy et al., 2022; Rohe et al., 2014; Sutka et al., 2008; Yang et al., 2014). Here, the dominance of N_2O production from ^{15}N–NO_3^-, combined with parallel natural abundance isotopomer studies, suggest that strains of denitrifying bacteria and fungi that produce N_2O with a high site preference may be important contributors to N_2O in the core of ODZs. The importance of N_2O production from NO_3^- also presents an important exception to the modular view of the microbial nitrogen cycle network, which holds that intermediates are passed externally from one cell to the next, rather than being held internally (Kuypers et al., 2018). N_2O production from NO_3^- that utilizes an internal NO_2^- pool is currently left out of most biogeochemical models of nitrogen cycling in and around oxygen-deficient zones (Bianchi et al., 2023), and modeling work that includes this as a source of N_2O is needed.

4.2 Pathways of hybrid N_2O production and implications for hybrid $\delta(^{15}N^{sp})$

Hybrid N_2O production peaked at the same depths as NH_3 oxidation (Fig. 6c, g, k), which were also the depths at which ammonia-oxidizing archaea were most abundant (Frey et al., 2023), consistent with N_2O production associated with ammonia-oxidizing archaea. At most stations and depths, the production of $^{45}N_2O^{\alpha}$ and $^{45}N_2O^{\beta}$ in both the ^{15}N–NO_2^- and ^{15}N–NH_4^+ experiments were roughly equal. From this we conclude that, during hybrid formation, N^{α} and N^{β} each retained nitrogen atoms derived from both NH_4^+ and NO_2^-. The equal formation of $^{45}N_2O^{\alpha}$ and $^{45}N_2O^{\beta}$ led to values of f

within an error of 0.5 in most of our experiments (Table S4), and the mean value of f across all stations and depths was 0.5 ± 0.2. This means that, during hybrid N_2O production, half of the N^{α} atoms were derived from NO_2^- and half were derived from NH_4^+ (likewise for N^{β}).

Although our data do not allow us to comment directly on the enzymatic machinery of hybrid N_2O formation, our data can be used to theorize hypothetical pathways for hybrid N_2O production. Firstly, we see much higher rates of hybrid production using ambient NO_2^- (Pathway 3 in Wan et al., 2023b) than hybrid production using cellular NO_2^- (Pathway 2 in Wan et al., 2023b). Again, this agrees with the results of Wan et al. (2023b), who see higher rates of hybrid formation from extracellular NO_2^- within the range of $[^{15}N\text{–}NH_4^+]/[NO_2^-]$ covered by our experiments. In our model, hybrid N_2O production is operationally defined as a 1:1 combination of N derived from NH_4^+ and NO_2^-, which is generally consistent with previous work (Stieglmeier et al., 2014). Any combination of N derived from NO_2^- with a second N derived from NO_2^- would be included in the modeled quantity of N_2O production from NO_2^-; likewise, any combination of N derived from NH_4^+ with a second N derived from NH_4^+ would be included in the N_2O production solely from NH_4^+. The question, then, is what reaction would be specific enough to have one N derived from each substrate but not specific enough to govern ^{15}N placement in the resulting N_2O? One such reaction could be the combination of NH_4^+ and NO_2^- to form a symmetrical intermediate such as hyponitrous acid (HONNOH, or hyponitrite $^-ONNO^-$ in its deprotonated form), which has been discussed as a possible intermediate in hybrid nitrous oxide formation (Wei et al., 2019). Hyponitrous acid may react to form N_2O via breakage of one of the N–O bonds, resulting in N_2O that contains a 1 : 1 ratio of NH_4^+:NO_2^-. With a precursor such as hyponitrite or hyponitrous acid, equal formation of $^{45}N_2O^{\alpha}$ and $^{45}N_2O^{\beta}$ could be achieved with non-selective N–O bond breakage.

These findings of equal $^{45}N_2O$ production have important implications for the natural abundance $\delta(^{15}N^{sp})$ of N_2O produced by the hybrid N_2O process. Assuming that hybrid N_2O production proceeds through a symmetrical intermediate in which NH_4^+ and NO_2^- are paired in a 1 : 1 ratio, we can model $\delta(^{15}N^{sp})$ as

$$\begin{aligned}\delta\left(^{15}N^{sp}\right) &= \delta\left(^{15}N^{\alpha}\right) - \delta\left(^{15}N^{\beta}\right)\\ &= \left[f\,\delta\left(^{15}N\text{–}NO_2^-\right) + (1-f)\,\delta\left(^{15}N\text{–}NH_4^+\right)\right]\\ &\quad -\left[(1-f)\,\delta\left(^{15}N\text{–}NO_2^-\right) + f\,\delta\left(^{15}N\text{–}NH_4^+\right) - \varepsilon\right], \quad (24)\end{aligned}$$

where f is the proportion of the α nitrogen derived from NO_2^- and the proportion of the β nitrogen derived from NH_4^+ and ε is the fractionation factor associated with N^{β}–O bond breakage. If $f \neq 1/2$, hybrid $\delta(^{15}N^{sp})$ retains a dependence on the $\delta(^{15}N)$ of the substrates – or, more accurately, the difference in $\delta(^{15}N)$ of the two substrates; if the $\delta(^{15}N)$ of the substrates is equal, it will cancel out regardless of f.

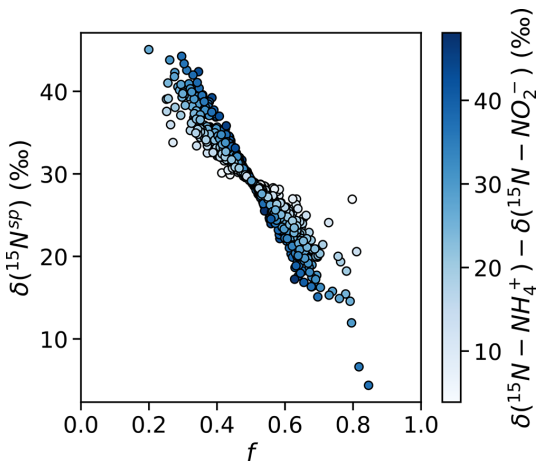

Figure 10. Simulated values of $\delta(^{15}N^{sp})$ calculated with a range of f (the proportion of N^{α} derived from NO_2^- during hybrid N_2O production) and $\delta(^{15}N\text{–}NH_4^+)$–$\delta(^{15}N\text{–}NO_2^-)$, assuming $\varepsilon = 30.3\,‰$ (Santoro et al., 2011). Results are shaded by $\delta(^{15}N\text{–}NH_4^+) - \delta(^{15}N\text{–}NO_2^-)$. When f is less than or greater than 1/2, there is the potential for $\delta(^{15}N^{sp})$ to depend on the isotopic compositions of each substrate.

If $\delta(^{15}N\text{–}NH_4^+) > \delta(^{15}N\text{–}NO_2^-)$, as is generally the case in the secondary nitrite maximum (Buchwald et al., 2015; Casciotti, 2016), then low values of f should produce high hybrid $\delta(^{15}N^{sp})$ and high values of f should produce low hybrid $\delta(^{15}N^{sp})$ (Fig. 10). If, however, $f = 1/2$, as was the case for most experimental depths in this study, hybrid $\delta(^{15}N^{sp})$ should depend only on ε and not on the isotopic composition of each substrate. This means that a $\delta(^{15}N^{sp})$ endmember could potentially be established for hybrid N_2O production, even though hybrid N_2O production draws from different substrate pools. Wei et al. (2019) discuss possible pathways or endmembers of hybrid N_2O formation, i.e., via *cis*-hyponitrous acid, *trans*-hyponitrous acid, and nitramide, all leading to N_2O with different $\delta(^{15}N^{sp})$ values. More studies are needed to determine the $\delta(^{15}N^{sp})$ of N_2O produced by ammonia-oxidizing archaea under a range of conditions.

The unequal production of $^{45}N_2O^{\alpha}$ and $^{45}N_2O^{\beta}$ observed at certain depths led to values of f significantly different from 0.5 (Table S4). At these depths, N^{α} retained a different proportion of nitrogen derived from NO_2^- and NH_4^+ than N^{β} did, causing $^{45}N_2O^{\alpha}$ and $^{45}N_2O^{\beta}$ to diverge. The depths with $f \neq 0.5$ anchored significant relationships between f and ambient $[O_2]$ ($R^2 = 0.84$, $p < 0.001$; Fig. S10a) and potential density anomaly (σ_θ) ($R^2 = 0.72$, $p < 0.001$; Fig. S10b). The oxygen and potential density gradients may be proxies for changing archaeal community compositions at different depths in the water column, which may exhibit different patterns of incorporation of NO_2^--derived N and NH_4^+-derived N into N^{α} and N^{β}. It is also possible that we sampled a different "hybrid" N_2O-producing process at these depths, such as fungal co-denitrification (Shoun et al., 2012), which may

proceed via a different pathway from archaeal hybrid N_2O production.

4.3 Rates of nitrification and N_2O production solely from NH_4^+

The rates of N_2O production from NH_4^+ in this study (i.e., the sum of hybrid N_2O production and N_2O production solely from NH_4^+) peaked at 240 ± 80 pM $N_2O\,d^{-1}$ (Table S4). These were similar to those measured on the same cruise by Frey et al. (2023), who measured rates of N_2O production from NH_4^+ in the oxycline of 28–149 pM $N_2O\,d^{-1}$ (Frey et al., 2023). The low rates of NH_3 oxidation to NO_2^- in this study (0.05–4.68 nM $N\,d^{-1}$) were also similar to those measured by Frey et al. (2023), who measured NH_3 oxidation rates of 1.0–11.7 nM d^{-1} in the oxycline. NH_3 oxidation rates in this study were smaller than those measured on the same cruise by Travis et al. (2023), who measured NH_3 oxidation rates as high as 90 ± 2 nM d^{-1} in fully oxygenated incubations at station PS3. The highest rates of NO_2^- oxidation we observed occurred at anoxic depths at stations PS2 and PS3 (Fig. 3e, h), which agrees with mounting evidence suggesting the importance of NO_2^- oxidation in apparently anoxic regions (Sun et al., 2017, 2021b).

When $[O_2]$ was less than 10 µM, the rates of hybrid N_2O production (6–230 pM $N_2O\,d^{-1}$) were orders of magnitude greater than the rates of N_2O production solely from NH_4^+ at the same depths (0–8 pM $N_2O\,d^{-1}$) (Fig. 6). Indeed, at the upper oxic–anoxic interface, the rates of hybrid N_2O production were on a similar order of magnitude to N_2O production from NO_2^- via denitrification (8–510 pM $N_2O\,d^{-1}$). These results agree with previous work showing that hybrid N_2O formation represents a high percentage of total N_2O production from NH_4^+ in the ETNP and eastern tropical South Pacific (ETSP) (Frey et al., 2020, 2023). The results in this study also agree with recent culture work: the ^{15}N–NH_4^+ experiments in this study fell along a range of $[^{15}N$–$NH_4^+] / [NO_2^-]$ of 0.14–0.5, in which Wan et al. (2023b) found that hybrid N_2O production occurred at a rate 2 to 4 times greater than N_2O production via hydroxylamine oxidation (N derived solely from NH_4^+) in cultures of *Nitrosopumilus maritimus*.

We found three depths near the surface where hybrid production comprised a smaller percentage (0 %–68 %) of total N_2O production from NH_4^+ (Fig. 7a–c). Previous work in the ETNP found that hybrid N_2O production always comprised > 90 % of N_2O production from NH_4^+ (Frey et al., 2023), and, where our samples overlapped with this previous work, we observed similarly high proportions of hybrid production (Fig. 5). The depths where we observed a smaller proportion of hybrid production had not been sampled previously; it is possible that we sampled different microbial communities there, acclimated to different levels of NH_4^+, NO_2^-, and dissolved oxygen. We also found that hybrid N_2O formation generally comprised a small proportion of total N_2O production, which was dominated by N_2O production from NO_3^-, especially at suboxic depths (Fig. 7d–h). This is similar to previous findings from the ETSP, which showed that hybrid formation comprised 0 %–95 % of total N_2O production from NO_2^- along the natural $[O_2]$ gradient (Frey et al., 2020). This large range is due to the large range of rates of N_2O production from NO_2^-, which can occur at orders of magnitude higher or lower than hybrid N_2O production.

4.4 Oxygen dependence of N_2O production rates and yields

N_2O production from NO_2^- and NO_3^- exhibited exponential dependence on dissolved oxygen, albeit with smaller maximum rates than those found in the ETSP (Frey et al., 2020; Ji et al., 2015). Most surprising were the significant rates of N_2O production via denitrification at $[O_2] > 3$ µM (Fig. 8a–d), which has previously been suggested as the threshold above which denitrification ceases (Dalsgaard et al., 2014). These observations are particularly evident in the plots of N_2O production from NO_3^- vs. incubation $[O_2]$ (Fig. 8b), where positive, significant rates of N_2O production from NO_3^- were evident in incubations containing $[O_2]$ as high as 19.2 ± 0.8 µM (PS2 deep ODZ core experiment). One explanation for N_2O production via denitrification at such high levels of ambient dissolved oxygen is particle-associated denitrification (Bianchi et al., 2018; Smriga et al., 2021; Wan et al., 2023a). Fungal denitrification may also have contributed to these fluxes, since denitrifying fungi can tolerate a higher level of oxygen than their bacterial counterparts. Additionally, denitrifying microbial communities acclimatized to lower ambient $[O_2]$ may be able to continue to produce N_2O when $[O_2]$ is suddenly increased.

These results showed that N_2O production from NO_3^- can occur in $[O_2]$ as high as 19.2 ± 0.8 µM, which is similar to results from the ETSP showing that N_2O production from NO_3^- in manipulated $[O_2]$ can be as high as 30 µM (Frey et al., 2020). The volume of suboxic water in the ocean has been increasing over the last 50 years and will likely continue to expand over the 21st century (Oschlies et al., 2018; Schmidtko et al., 2017; Stramma et al., 2008), although the extent of this deoxygenation remains uncertain (Bianchi et al., 2018; Busecke et al., 2022; Cabré et al., 2015). Constraining the window of oxygen concentrations under which denitrification leads to N_2O production will be key to understanding how marine deoxygenation and N_2O cycling will interact.

While this study and others have found that hybrid N_2O production represents a consistent percentage of N_2O production from NH_4^+ along a range of ambient $[O_2]$ (Frey et al., 2020, 2023), the rate of hybrid N_2O production followed a clear exponential dependence on dissolved oxygen (Fig. 9). The differences in ambient and incubation $[O_2]$ resulted in slight differences in the coefficients for each yield curve; nevertheless, hybrid rates plotted along both ambient and incubation $[O_2]$ gradients exhibited remarkably similar $[O_2]$ inhi-

bition curves, with the highest rates at $[O_2] < 7$ µM. These results are similar to those of Frey et al. (2023), who showed a decrease in N_2O production from NH_4^+ with increasing $[O_2]$.

The maximum N_2O yield for hybrid production (21 %; Fig. 8c, d) was 1 order of magnitude higher than previous estimates of N_2O yields during NH_3 oxidation from ETSP and ETNP, which did not include hybrid N_2O production (Ji et al., 2018). These high yields occurred at the oxic–anoxic interface at station PS1 and just below the oxic–anoxic interface at station PS3, where ambient $[O_2]$ was below detection but NH_3 oxidation still occurred (Fig. 3). This indicates the potential for extremely high yields of N_2O from hybrid production where NH_3 oxidation is active in suboxic to anoxic environments.

N_2O yields during production solely from NH_4^+ also increased with decreasing $[O_2]$ (Fig. 9b), as previously reported (Frey et al., 2020; Goreau et al., 1980; Ji et al., 2018; Nevison et al., 2003). N_2O yields during production solely from NH_4^+ increased sharply with decreasing $[O_2]$ along both ambient and incubation $[O_2]$ gradients but were much smaller than the yields from hybrid N_2O production (Fig. 8c–d). The maximum yields during production solely from NH_4^+ were similar to the maximum yields found by another study in the ETNP, which were around 3 % (Frey et al., 2023), and much higher than yields from ammonia-oxidizing archaea in soils and culture (up to 0.03 %) (Hink et al., 2017a, b).

4.5 Experimental artifacts

Care was taken to minimize the effects of experimental setup on the microbial communities in each sample. In addition to the steps taken to prevent oxygen contamination (described in Sect. 2: Methods), a relatively short 24 h incubation period was selected to minimize bottle effects and shifts in the microbial community composition over the course of each incubation. Nonetheless, sample collection, preparation, and incubation conditions could have affected the microbial communities in several ways. Firstly, samples were frequently collected from depths where the water temperature was cooler than that of the laboratory, and, while samples were returned to a cool temperature during incubation (12 °C), they were exposed to warmer temperatures (> 20 °C) during the 2 h in which they underwent collection and manipulation prior to incubation. Likewise, during this interval, samples were exposed to higher light levels before being returned to the dark for incubation. While oxygen contamination was minimized during sample collection, it was not eliminated entirely, and a temporary oxygen intrusion before sparging may have poisoned certain anaerobic processes. The 90 min sparge also likely removed carbon dioxide in addition to oxygen and N_2O, increasing the pH of each sample. Finally, the NH_4^+ and NO_2^- tracer and carrier additions exceeded the ambient concentrations of these substrates, potentially stimulating the rates of processes that rely on these substrates. All of these perturbations, while common among incubation studies, may have affected the microbial community differentially in each sample. Thus, the results presented here represent processes able to withstand these perturbations to ambient environmental conditions. Any abiotic reactions between the $HgCl_2$ preservative and the NO_2^- tracer and carrier would have shifted all three time points equally and thus should not introduce a bias into the slopes of ^{15}N-labeled N_2O with time and the rates calculated from there.

4.6 Alternative sources of N_2O

Other processes may have contributed to N_2O production in our samples. A complementary set of experiments found that fungal denitrification comprised 50 % of total N_2O production via denitrification at the secondary chlorophyll *a* maximum depths discussed here (Peng and Valentine, 2021). Additionally, since our samples were unfiltered, particle-associated N_2O production and consumption may have occurred in some of our experiments, especially in experiments at the highly productive coastal station. We cannot rule out any of these alternative sources of N_2O in our samples, so we regard these processes as potential contributors to the bulk denitrifying flux discussed here.

5 Conclusions

We applied N_2O isotopocule measurements to ^{15}N tracer incubations to measure N_2O production rates and mechanisms in the ETNP. We found that N_2O production rates peaked at the oxic–anoxic interface above the ODZ, with the highest rates of N_2O production from NO_3^-. Hybrid N_2O production peaked in both the shallow and deep oxyclines, where NH_3 oxidation was also active, and exhibited yields as high as 21 % of ammonia oxidation.

Based on the equal production of $^{45}N_2O^{\alpha}$ and $^{45}N_2O^{\beta}$ in the vast majority of our experiments, we posit a two-step process for hybrid N_2O production involving an initial bond-forming step that draws nitrogen atoms from each substrate to form a symmetric intermediate and a second bond-breaking step that breaks an N–O bond in the symmetric intermediate to form N_2O. From this, we infer that hybrid N_2O production likely has a consistent $\delta(^{15}N^{sp})$, despite drawing from two distinct substrate pools. This has important implications for the interpretation of natural abundance isotopocule measurements, since it implies that it may be possible to define a $\delta(^{15}N^{sp})$ endmember for hybrid N_2O formation. More culture experiments are needed to quantify the $\delta(^{15}N^{sp})$ of N_2O produced by ammonia-oxidizing archaea under different temperatures, oxygen levels, and ratios of NH_4^+ / NO_2^-.

N_2O production rates and yields of every process examined here were inhibited by dissolved oxygen. The N_2O yield from hydroxylamine oxidation was most sensitive to

O_2, followed by the rates of N_2O production from NO_2^- via denitrification, hybrid N_2O production, and N_2O production from NO_3^- via denitrification. Indeed, we measured positive, significant rates of N_2O production from NO_3^- at ambient $[O_2]$ as high as 12.5 µM and at manipulated $[O_2]$ as high as 19.2 µM. These denitrifying fluxes may have derived partially from fungal N_2O production, since fungal denitrifiers can tolerate higher oxygen levels than bacteria (Peng and Valentine, 2021) or particle-associated denitrification (Bianchi et al., 2018; Smriga et al., 2021). These results suggest that a broad window of $[O_2]$ could support net N_2O accumulation, and additional studies are needed to further constrain this window and the resulting feedbacks between denitrification and marine deoxygenation.

Appendix A: Estimating uncertainties for nitrate isotope analyses from tracer samples

Since only 2 mL of sample was available for preparation and analysis of nitrate isotopes using the denitrifier method, it was not possible to always achieve consistent peak areas. Instead of discarding low-peak-area samples, however, we wanted to establish a method to estimate the uncertainties associated with individual samples based on their peak area. This uncertainty arises from a correction scheme for $\delta(^{15}N)$ that assumes constant blank : sample quantity ratios. What follows is a method for estimating this uncertainty, using the slope and intercept of the calibration curve and blank peak area.

In brief, the first step of this method is to calculate the peak area and $\delta(^{15}N)$ of the blank for an individual run (batch of bacteria) using the slope and intercept of the nitrate isotope calibration curve (Casciotti et al., 2002). Then, a range of theoretical measured $\delta(^{15}N)$ is calculated for a set of dummy samples based on a range of "actual" $\delta(^{15}N)$, a range of theoretical peak areas, and the peak area and $\delta(^{15}N)$ of the blank. Then, we correct each of these theoretical measured $\delta(^{15}N)$ values with the calibration curve, as one would do normally, to obtain $\delta(^{15}N_{corrected})$ for each dummy sample. We estimate the error for each dummy sample by comparing the $\delta(^{15}N_{corrected})$ we have calculated to the $\delta(^{15}N_{sample})$ we have assigned to it. Then, for each run (and associated blank), we can fit a function through these errors, their corresponding peak areas, and the corresponding $\delta(^{15}N_{sample})$. We can then feed this function the peak area and measured $\delta(^{15}N)$ of actual samples in that run to estimate their uncertainties.

In practice, we start with a simple mass balance that states that the measured $\delta(^{15}N)$ is a function of the sample $\delta(^{15}N)$, sample peak area A_{sample}, blank $\delta(^{15}N)$, and blank peak area A_{blank}:

$$\delta\left(^{15}N_{measured}\right)\left(A_{measured}\right) = \delta\left(^{15}N_{sample}\right)\left(A_{sample}\right) + \delta\left(^{15}N_{blank}\right)\left(A_{blank}\right), \quad \text{(A1)}$$

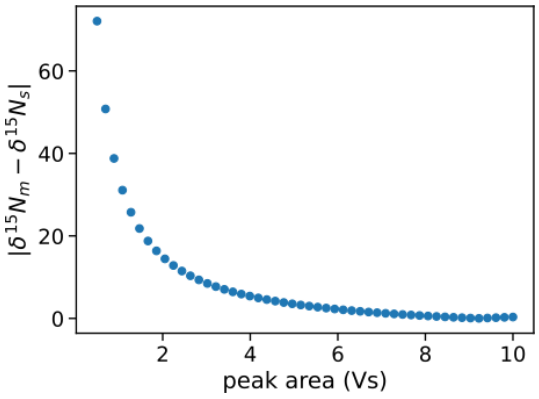

Figure A1. $\delta(^{15}N_{error})$ vs. peak area for a range of dummy samples with measured peak areas from 0.5 to 10 Vs, based on a blank peak area of 0.15 Vs and $\delta(^{15}N_{blank})$ of −69.3 ‰.

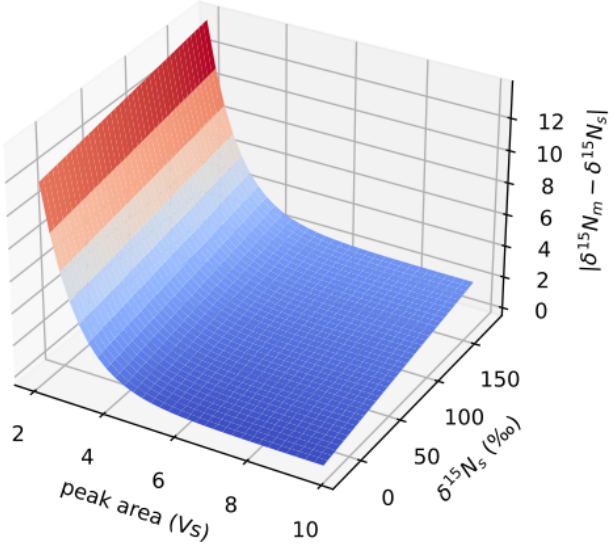

Figure A2. $\delta(^{15}N_{error})$ vs. peak area and $\delta(^{15}N_{sample})$ for a range of dummy samples with peak areas from 0.5 to 10 Vs and $\delta(^{15}N_{sample})$ from −20 ‰ to 180 ‰, based on a blank peak area of 0.15 Vs and $\delta(^{15}N_{blank})$ of −69.3 ‰.

where $\delta(^{15}N_{measured})$ is the measured $\delta(^{15}N)$, $A_{measured}$ is the measured peak area, $\delta(^{15}N_{sample})$ is the actual sample $\delta(^{15}N)$, A_{sample} is the peak area attributable to sample N, $\delta(^{15}N_{blank})$ is the $\delta(^{15}N)$ of the blank, and A_{blank} is the peak area attributable to blank N. Dividing through by $A_{measured}$,

$$\delta\left(^{15}N_{measured}\right) = \delta\left(^{15}N_{sample}\right)\left(\frac{A_{sample}}{A_{measured}}\right) + \delta\left(^{15}N_{blank}\right)\left(\frac{A_{blank}}{A_{measured}}\right). \quad \text{(A2)}$$

Equation (A2) can be expressed as a linear equation, $y = mx + b$, where m is the slope of $\delta\left(^{15}N_{measured}\right)$ vs.

$\delta\left({}^{15}\mathrm{N}_{\mathrm{sample}}\right)$ and b is the y intercept. Thus

$$m = \left(\frac{A_{\mathrm{sample}}}{A_{\mathrm{measured}}}\right) \tag{A3}$$

$$b = \delta\left({}^{15}\mathrm{N}_{\mathrm{blank}}\right)\left(\frac{A_{\mathrm{blank}}}{A_{\mathrm{measured}}}\right). \tag{A4}$$

We can obtain the mean blank peak area A_{blank} from the slope and the mean peak area of the measured reference materials (A_{measured}):

$$\left(\frac{A_{\mathrm{blank}}}{A_{\mathrm{measured}}}\right) = 1 - \left(\frac{A_{\mathrm{sample}}}{A_{\mathrm{measured}}}\right) = 1 - (m) \tag{A5}$$

$$A_{\mathrm{blank}} = [1 - (m)]\,(A_{\mathrm{measured}}). \tag{A6}$$

Finally, we obtain $\delta({}^{15}\mathrm{N}_{\mathrm{blank}})$ from

$$\delta\left({}^{15}\mathrm{N}_{\mathrm{blank}}\right) = b/\left(\frac{A_{\mathrm{blank}}}{A_{\mathrm{measured}}}\right) = \frac{b}{1 - (m)}. \tag{A7}$$

We assign the dummy samples a range of theoretical measured peak areas, A_{measured}. The ratio of the blank peak area to the measured peak areas for a given sample is given by dividing A_{blank} (calculated from Eq. A6) by this theoretical peak area to obtain $\left(\frac{A_{\mathrm{blank}}}{A_{\mathrm{measured},i}}\right)$, where $A_{\mathrm{measured},i}$ is the theoretical peak area for that sample. Then, the ratio of sample peak area to measured peak area for a given theoretical sample is given by

$$\left(\frac{A_{\mathrm{sample}}}{A_{\mathrm{measured},i}}\right) = 1 - \left(\frac{A_{\mathrm{blank}}}{A_{\mathrm{measured},i}}\right). \tag{A8}$$

As a first example, we assign all of the theoretical samples the same $\delta({}^{15}\mathrm{N}_{\mathrm{sample}})$ of 180 ‰. Then, to obtain a range of theoretical measured $\delta({}^{15}\mathrm{N}_{\mathrm{measured}})$, we plug the $\delta({}^{15}\mathrm{N}_{\mathrm{blank}})$ calculated from Eq. (A7), the range of theoretical peak areas $A_{\mathrm{measured,i}}$, and this $\delta({}^{15}\mathrm{N}_{\mathrm{sample}})$ into Eq. (A2):

$$\delta\left({}^{15}\mathrm{N}_{\mathrm{measured}_i}\right) = 180‰ \cdot \left(\frac{A_{\mathrm{sample}}}{A_{\mathrm{measured},i}}\right) + \delta\left({}^{15}\mathrm{N}_{\mathrm{blank}}\right)\left(\frac{A_{\mathrm{blank}}}{A_{\mathrm{measured},i}}\right). \tag{A9}$$

We correct the range of $\delta\left({}^{15}\mathrm{N}_{\mathrm{measured}_i}\right)$ calculated from Eq. (A9) with the slope and intercept of the calibration curve $\delta\left({}^{15}\mathrm{N}_{\mathrm{sample}}\right)$ vs. $\delta\left({}^{15}\mathrm{N}_{\mathrm{measured}}\right)$:

$$\delta\left({}^{15}\mathrm{N}_{\mathrm{corrected}_i}\right) = m\left(\frac{A_{\mathrm{sample}}}{A_{\mathrm{measured},i}}\right) + b. \tag{A10}$$

Then we calculate the error associated with each dummy sample using

$$\delta\left({}^{15}\mathrm{N}_{\mathrm{error}}\right) = \left|\delta\left({}^{15}\mathrm{N}_{\mathrm{corrected}_i}\right) - 180‰\right|. \tag{A11}$$

Following this exercise with a range of theoretical peak areas from 0.5 to 10 Vs produces the following curve (Fig. A1). It shows that these theoretical errors increase as peak area decreases, reflecting the basis of the error.

Repeating this exercise with a range of $\delta({}^{15}\mathrm{N}_{\mathrm{sample}})$ values from −20 ‰ to 180 ‰ produces a 3D version of this curve (Fig. A2). This shows that the estimated uncertainty is highest for samples with $\delta({}^{15}\mathrm{N}_{\mathrm{sample}})$ most divergent from $\delta({}^{15}\mathrm{N}_{\mathrm{blank}})$ and for the peak areas most divergent from the reference materials.

Finally, we fit a function of the following form through these theoretical data:

$$\delta\left({}^{15}\mathrm{N}_{\mathrm{error}}\right) = a \cdot e^{c \cdot A_{\mathrm{sample}}} + d \cdot \delta\left({}^{15}\mathrm{N}_{\mathrm{sample}}\right), \tag{A12}$$

where a, c, and d are constants, A_{sample} is the measured peak areas of the theoretical samples, and $\delta({}^{15}\mathrm{N}_{\mathrm{sample}})$ is the assigned value for the dummy samples.

This procedure was repeated for each denitrifier run to produce coefficients a, c, and d specific to that set of analyses. Then, to estimate the uncertainty associated with each measurement, we used the corrected $\delta({}^{15}\mathrm{N})$ for each sample's $\delta({}^{15}\mathrm{N}_{\mathrm{sample}})$ and its measured peak area for A_{sample} in Eq. (A12).

Code and data availability. The data reported in this study can be found in the Stanford Digital Repository (https://doi.org/10.25740/ss974md4840, Kelly and Casciotti, 2023). Forward-running model code is available via Zenodo (https://doi.org/10.5281/zenodo.11475416; Kelly, 2024). pyisotopomer, which was used for N_2O isotopocule data corrections, is available for installation from the Python Package Index and Zenodo (https://doi.org/10.5281/zenodo.7552724; Kelly, 2023).

Supplement. The supplement related to this article is available online at: https://doi.org/10.5194/bg-21-3215-2024-supplement.

Author contributions. CLK and KLC conceptualized the study, with input from CF and BBW. CLK and NMT carried out the experiments at sea, with assistance and supervision from CF and BBW. CLK and PAB analyzed the incubation samples in the laboratory. CLK performed the formal analysis of the data, developed the model code, and performed the model optimizations. XS provided N_2O consumption data for inclusion in the model. KLC acquired funding for the study. CLK prepared the article with contributions from all co-authors.

Competing interests. The contact author has declared that none of the authors has any competing interests.

Disclaimer. Publisher's note: Copernicus Publications remains neutral with regard to jurisdictional claims made in the text, published maps, institutional affiliations, or any other geographical representation in this paper. While Copernicus Publications makes ev-

ery effort to include appropriate place names, the final responsibility lies with the authors.

Special issue statement. This article is part of the special issue "Low-oxygen environments and deoxygenation in open and coastal marine waters". It is not associated with a conference.

Acknowledgements. We would like to thank Stanford University and the Stanford Research Computing Center for providing computational resources and support that contributed to this research. We would also like to thank Julie Granger, Scott Wankel, and two anonymous reviewers for their constructive feedback during the review process. This research was supported by US NSF grant no. OCE-1657868 to Karen L. Casciotti. Colette L. Kelly was supported by an NSF Graduate Research Fellowship. The authors declare no competing financial interests.

Financial support. This research has been supported by the Directorate for Geosciences (grant no. OCE-1657868).

Review statement. This paper was edited by Nicolas Brüggemann and reviewed by Scott Wankel and two anonymous referees.

References

Babbin, A. R., Bianchi, D., Jayakumar, A., and Ward, B. B.: Rapid nitrous oxide cycling in the suboxic ocean, Science, 348, 1127–1129, https://doi.org/10.1126/science.aaa8380, 2015.

Bianchi, D., Weber, T. S., Kiko, R., and Deutsch, C.: Global niche of marine anaerobic metabolisms expanded by particle microenvironments, Nat. Geosci., 11, 263–268, https://doi.org/10.1038/s41561-018-0081-0, 2018.

Bianchi, D., McCoy, D., and Yang, S.: Formulation, optimization, and sensitivity of NitrOMZv1.0, a biogeochemical model of the nitrogen cycle in oceanic oxygen minimum zones, Geosci. Model Dev., 16, 3581–3609, https://doi.org/10.5194/gmd-16-3581-2023, 2023.

Böhlke, J. K., Mroczkowski, S. J., and Coplen, T. B.: Oxygen isotopes in nitrate: new reference materials for $^{18}O:^{17}O:^{16}O$ measurements and observations on nitrate-water equilibration, Rapid Commun. Mass Sp., 17, 1835–1846, https://doi.org/10.1002/rcm.1123, 2003.

Bourbonnais, A., Letscher, R. T., Bange, H. W., Échevin, V., Larkum, J., Mohn, J., Yoshida, N., and Altabet, M. A.: N_2O production and consumption from stable isotopic and concentration data in the Peruvian coastal upwelling system, Global Biogeochem. Cy., 31, 678–698, https://doi.org/10.1002/2016GB005567, 2017.

Bourbonnais, A., Chang, B. X., Sonnerup, R. E., Doney, S. C., and Altabet, M. A.: Marine N_2O cycling from high spatial resolution concentration, stable isotopic and isotopomer measurements along a meridional transect in the eastern Pacific Ocean, Front. Mar. Sci., 10, 1137064, https://doi.org/10.3389/fmars.2023.1137064, 2023.

Breitburg, D., Levin, L. A., Oschlies, A., Grégoire, M., Chavez, F. P., Conley, D. J., Garçon, V., Gilbert, D., Gutiérrez, D., Isensee, K., Jacinto, G. S., Limburg, K. E., Montes, I., Naqvi, S. W. A., Pitcher, G. C., Rabalais, N. N., Roman, M. R., Rose, K. A., Seibel, B. A., Telszewski, M., Yasuhara, M., and Zhang, J.: Declining oxygen in the global ocean and coastal waters, Science, 359, eaam7240, https://doi.org/10.1126/science.aam7240, 2018.

Brenninkmeijer, C. A. M. and Röckmann, T.: Mass spectrometry of the intramolecular nitrogen isotope distribution of environmental nitrous oxide using fragment-ion analysis, Rapid Commun. Mass Sp., 13, 2028–2033, https://doi.org/10.1002/(SICI)1097-0231(19991030)13:20<2028::AID-RCM751>3.0.CO;2-J, 1999.

Buchwald, C., Santoro, A. E., Stanley, R. H. R., and Casciotti, K. L.: Nitrogen cycling in the secondary nitrite maximum of the eastern tropical North Pacific off Costa Rica, Gloal Biogeochem. Cy., 29, 2061–2081, https://doi.org/10.1002/2015GB005187, 2015.

Busecke, J. J. M., Resplandy, L., Ditkovsky, S. J., and John, J. G.: Diverging Fates of the Pacific Ocean Oxygen Minimum Zone and Its Core in a Warming World, AGU Adv., 3, e2021AV000470, https://doi.org/10.1029/2021AV000470, 2022.

Cabré, A., Marinov, I., Bernardello, R., and Bianchi, D.: Oxygen minimum zones in the tropical Pacific across CMIP5 models: mean state differences and climate change trends, Biogeosciences, 12, 5429–5454, https://doi.org/10.5194/bg-12-5429-2015, 2015.

Carini, P., Dupont, C. L., and Santoro, A. E.: Patterns of thaumarchaeal gene expression in culture and diverse marine environments, Environ. Microbiol., 20, 2112–2124, https://doi.org/10.1111/1462-2920.14107, 2018.

Casciotti, K. L.: Nitrite isotopes as tracers of marine N cycle processes, Philos. T. R. Soc. A, 374, 20150295, https://doi.org/10.1098/rsta.2015.0295, 2016.

Casciotti, K. L., Sigman, D. M., Hastings, M. G., Böhlke, J. K., and Hilkert, A.: Measurement of the Oxygen Isotopic Composition of Nitrate in Seawater and Freshwater Using the Denitrifier Method, Anal. Chem., 74, 4905–4912, https://doi.org/10.1021/ac020113w, 2002.

Casciotti, K. L., Böhlke, J. K., McIlvin, M. R., Mroczkowski, S. J., and Hannon, J. E.: Oxygen Isotopes in Nitrite: Analysis, Calibration, and Equilibration, Anal. Chem., 79, 2427–2436, https://doi.org/10.1021/ac061598h, 2007.

Casciotti, K. L., Forbes, M., Vedamati, J., Peters, B. D., Martin, T. S., and Mordy, C. W.: Nitrous oxide cycling in the Eastern Tropical South Pacific as inferred from isotopic and isotopomeric data, Deep-Sea Res. Pt. II, 156, 155–167, https://doi.org/10.1016/j.dsr2.2018.07.014, 2018.

Codispoti, L. A. and Christensen, J. P.: Nitrification, denitrification and nitrous oxide cycling in the eastern tropical South Pacific ocean, Mar. Chem., 16, 277–300, https://doi.org/10.1016/0304-4203(85)90051-9, 1985.

Cohen, Y. and Gordon, L. I.: Nitrous oxide production in the Ocean, J. Geophys. Res.-Ocean., 84, 347–353, https://doi.org/10.1029/JC084iC01p00347, 1979.

Dalsgaard, T., Stewart, F. J., Thamdrup, B., Brabandere, L. D., Revsbech, N. P., Ulloa, O., Canfield, D. E., and DeLong, E. F.: Oxygen at Nanomolar Levels Reversibly Suppresses Process Rates and Gene Expression in Anammox and Denitrifica-

tion in the Oxygen Minimum Zone off Northern Chile, mBio, 5, e01966-14, https://doi.org/10.1128/mBio.01966-14, 2014.

Farías, L., Castro-González, M., Cornejo, M., Charpentier, J., Faúndez, J., Boontanon, N., and Yoshida, N.: Denitrification and nitrous oxide cycling within the upper oxycline of the eastern tropical South Pacific oxygen minimum zone, Limnol. Oceanogr., 54, 132–144, https://doi.org/10.4319/lo.2009.54.1.0132, 2009.

Farías, L., Faúndez, J., Fernández, C., Cornejo, M., Sanhueza, S., and Carrasco, C.: Biological N_2O fixation in the Eastern South Pacific Ocean and marine cyanobacterial cultures, PloS One, 8, e63956, https://doi.org/10.1371/journal.pone.0063956, 2013.

Frame, C. H. and Casciotti, K. L.: Biogeochemical controls and isotopic signatures of nitrous oxide production by a marine ammonia-oxidizing bacterium, Biogeosciences, 7, 2695–2709, https://doi.org/10.5194/bg-7-2695-2010, 2010.

Frame, C. H., Lau, E., Nolan, E. J. I., Goepfert, T. J., and Lehmann, M. F.: Acidification Enhances Hybrid N_2O Production Associated with Aquatic Ammonia-Oxidizing Microorganisms, Front. Microbiol., 7, 2104, https://doi.org/10.3389/fmicb.2016.02104, 2017.

Frey, C., Bange, H. W., Achterberg, E. P., Jayakumar, A., Löscher, C. R., Arévalo-Martínez, D. L., León-Palmero, E., Sun, M., Sun, X., Xie, R. C., Oleynik, S., and Ward, B. B.: Regulation of nitrous oxide production in low-oxygen waters off the coast of Peru, Biogeosciences, 17, 2263–2287, https://doi.org/10.5194/bg-17-2263-2020, 2020.

Frey, C., Sun, X., Szemberski, L., Casciotti, K. L., Garcia-Robledo, E., Jayakumar, A., Kelly, C. L., Lehmann, M. F., and Ward, B. B.: Kinetics of nitrous oxide production from ammonia oxidation in the Eastern Tropical North Pacific, Limnol. Oceanogr., 68, 424–438, https://doi.org/10.1002/lno.12283, 2023.

Garcia, H. E. and Gordon, L. I.: Oxygen Solubility in Seawater: Better Fitting Equations, Limnol. Oceanogr., 37, 1307–1312, 1992.

Goreau, T. J., Kaplan, W. A., Wofsy, S. C., McElroy, M. B., Valois, F. W., and Watson, S. W.: Production of NO_2^- and N_2O by Nitrifying Bacteria at Reduced Concentrations of Oxygen, Appl. Environ. Microbiol., 40, 526–532, https://doi.org/10.1128/aem.40.3.526-532.1980, 1980.

Granger, J. and Sigman, D. M.: Removal of nitrite with sulfamic acid for nitrate N and O isotope analysis with the denitrifier method, Rapid Commun. Mass Sp., 23, 3753–3762, https://doi.org/10.1002/rcm.4307, 2009.

Grasshoff, K., Ehrhardt, M., Kremling, K., and Anderson, L. G. (Eds.): Methods of seawater analysis, 3rd, completely rev. and extended ed ed., Wiley-VCH, Weinheim, New York, 600 pp., 1999.

Hink, L., Nicol, G. W., and Prosser, J. I.: Archaea produce lower yields of N $_2$ O than bacteria during aerobic ammonia oxidation in soil: N $_2$ O production by soil ammonia oxidisers, Environ. Microbiol., 19, 4829–4837, https://doi.org/10.1111/1462-2920.13282, 2017a.

Hink, L., Lycus, P., Gubry-Rangin, C., Frostegård, Å., Nicol, G. W., Prosser, J. I., and Bakken, L. R.: Kinetics of NH3-oxidation, NO-turnover, N_2O-production and electron flow during oxygen depletion in model bacterial and archaeal ammonia oxidisers, Environ. Microbiol., 19, 4882–4896, https://doi.org/10.1111/1462-2920.13914, 2017b.

Holmes, R. M., Aminot, A., Kérouel, R., Hooker, B. A., and Peterson, B. J.: A simple and precise method for measuring ammonium in marine and freshwater ecosystems, Can. J. Fish. Aquat. Sci., 56, 1801–1808, https://doi.org/10.1139/f99-128, 1999.

Ji, Q., Babbin, A. R., Jayakumar, A., Oleynik, S., and Ward, B. B.: Nitrous oxide production by nitrification and denitrification in the Eastern Tropical South Pacific oxygen minimum zone, Geophys. Res. Lett., 42, 10755–10764, https://doi.org/10.1002/2015GL066853, 2015.

Ji, Q., Buitenhuis, E., Suntharalingam, P., Sarmiento, J. L., and Ward, B. B.: Global Nitrous Oxide Production Determined by Oxygen Sensitivity of Nitrification and Denitrification, Global Biogeochem. Cy., 32, 1790–1802, https://doi.org/10.1029/2018GB005887, 2018.

Kaiser, J., Park, S., Boering, K. A., Brenninkmeijer, C. A. M., Hilkert, A., and Röckmann, T.: Mass spectrometric method for the absolute calibration of the intramolecular nitrogen isotope distribution in nitrous oxide, Anal. Bioanal. Chem., 378, 256–269, https://doi.org/10.1007/s00216-003-2233-2, 2004.

Kantnerová, K., Hattori, S., Toyoda, S., Yoshida, N., Emmenegger, L., Bernasconi, S. M., and Mohn, J.: Clumped isotope signatures of nitrous oxide formed by bacterial denitrification, Geochim. Cosmochim. Ac., 328, 120–129, https://doi.org/10.1016/j.gca.2022.05.006, 2022.

Kelly, C. L.: ckelly314/pyisotopomer: v1.0.4, Zenodo [code], https://doi.org/10.5281/zenodo.7552724, 2023.

Kelly, C. L.: ckelly314/isotopomer-soup: Second release of isotopomer-soup (v0.0.2), Zenodo [code], https://doi.org/10.5281/zenodo.11475416, 2024.

Kelly, C. L. and Casciotti, K. L.: Data in support of "Isotopomer labeling and oxygen dependence of hybrid nitrous oxide production" from the Eastern Tropical North Pacific, Stanford Digital Repository [data set], https://doi.org/10.25740/ss974md4840, 2023.

Kelly, C. L., Travis, N. M., Baya, P. A., and Casciotti, K. L.: Quantifying Nitrous Oxide Cycling Regimes in the Eastern Tropical North Pacific Ocean With Isotopomer Analysis, Global Biogeochem. Cy., 35, e2020GB006637, https://doi.org/10.1029/2020GB006637, 2021.

Kelly, C. L., Manning, C., Frey, C., Kaiser, J., Gluschankoff, N., and Casciotti, K. L.: Pyisotopomer: A Python package for obtaining intramolecular isotope ratio differences from mass spectrometric analysis of nitrous oxide isotopocules, Rapid Commun. Mass Sp., 37, e9513, https://doi.org/10.1002/rcm.9513, 2023.

Kim, K.-R. and Craig, H.: Two-isotope characterization of N_2O in the Pacific Ocean and constraints on its origin in deep water, Nature, 347, 58–61, https://doi.org/10.1038/347058a0, 1990.

Kozlowski, J. A., Kits, K. D., and Stein, L. Y.: Comparison of Nitrogen Oxide Metabolism among Diverse Ammonia-Oxidizing Bacteria, Front. Microbiol., 7, 1090, https://doi.org/10.3389/fmicb.2016.01090, 2016.

Kraft, B., Jehmlich, N., Larsen, M., Bristow, L. A., Könneke, M., Thamdrup, B., and Canfield, D. E.: Oxygen and nitrogen production by an ammonia-oxidizing archaeon, Science, 375, 97–100, https://doi.org/10.1126/science.abe6733, 2022.

Kuypers, M. M. M., Marchant, H. K., and Kartal, B.: The microbial nitrogen-cycling network, Nat. Rev. Microbiol., 16, 263–276, https://doi.org/10.1038/nrmicro.2018.9, 2018.

Lancaster, K. M., Caranto, J. D., Majer, S. H., and Smith, M. A.: Alternative Bioenergy: Updates to and Challenges

in Nitrification Metalloenzymology, Joule, 2, 421–441, https://doi.org/10.1016/j.joule.2018.01.018, 2018.

Lazo-Murphy, B. M., Larson, S., Staines, S., Bruck, H., McHenry, J., Bourbonnais, A., and Peng, X.: Nitrous oxide production and isotopomer composition by fungi isolated from salt marsh sediments, Front. Mar. Sci., 9, 1098508, https://doi.org/10.3389/fmars.2022.1098508, 2022.

Lipschultz, F.: Chap. 31 – Isotope Tracer Methods for Studies of the Marine Nitrogen Cycle, in: Nitrogen in the Marine Environment, 2nd Edn., edited by: Capone, D. G., Bronk, D. A., Mulholland, M. R., and Carpenter, E. J., Academic Press, San Diego, 1345–1384, https://doi.org/10.1016/B978-0-12-372522-6.00031-1, 2008.

Magyar, P. M., Orphan, V. J., and Eiler, J. M.: Measurement of rare isotopologues of nitrous oxide by high-resolution multi-collector mass spectrometry, Rapid Commun. Mass Sp., 30, 1923–1940, https://doi.org/10.1002/rcm.7671, 2016.

Martens-Habbena, W., Qin, W., Horak, R. E. A., Urakawa, H., Schauer, A. J., Moffett, J. W., Armbrust, E. V., Ingalls, A. E., Devol, A. H., and Stahl, D. A.: The production of nitric oxide by marine ammonia-oxidizing archaea and inhibition of archaeal ammonia oxidation by a nitric oxide scavenger, Environ. Microbiol., 17, 2261–2274, https://doi.org/10.1111/1462-2920.12677, 2015.

McIlvin, M. R. and Altabet, M. A.: Chemical Conversion of Nitrate and Nitrite to Nitrous Oxide for Nitrogen and Oxygen Isotopic Analysis in Freshwater and Seawater, Anal. Chem., 77, 5589–5595, https://doi.org/10.1021/ac050528s, 2005.

McIlvin, M. R. and Casciotti, K. L.: Fully automated system for stable isotopic analyses of dissolved nitrous oxide at natural abundance levels, Limnol. Oceanogr. Method., 8, 54–66, https://doi.org/10.4319/lom.2010.8.54, 2010.

McIlvin, M. R. and Casciotti, K. L.: Technical updates to the bacterial method for nitrate isotopic analyses, Anal. Chem., 83, 1850–1856, https://doi.org/10.1021/ac1028984, 2011.

Monreal, P. J., Kelly, C. L., Travis, N. M., and Casciotti, K. L.: Identifying the Sources and Drivers of Nitrous Oxide Accumulation in the Eddy-Influenced Eastern Tropical North Pacific Oxygen-Deficient Zone, Global Biogeochem. Cy., 36, e2022GB007310, https://doi.org/10.1029/2022GB007310, 2022.

Naqvi, S. W. A., Jayakumar, D. A., Narvekar, P. V., Naik, H., Sarma, V. V. S. S., D'Souza, W., Joseph, S., and George, M. D.: Increased marine production of N_2O due to intensifying anoxia on the Indian continental shelf, Nature, 408, 346–349, https://doi.org/10.1038/35042551, 2000.

Nelder, J. A. and Mead, R.: A Simplex Method for Function Minimization, Comput. J., 7, 308–313, https://doi.org/10.1093/comjnl/7.4.308, 1965.

Nevison, C., Butler, J. H., and Elkins, J. W.: Global distribution of N_2O and the Delta N_2O-AOU yield in the subsurface ocean, Global Biogeochem. Cy., 17, 1119, https://doi.org/10.1029/2003GB002068, 2003.

NOAA/National Weather Service: Cold and Warm Episodes by Season, National Weather Service Climate Prediction Center [data set], https://origin.cpc.ncep.noaa.gov/products/analysis_monitoring/ensostuff/ONI_v5.php, last access: 20 July 2020.

Oschlies, A., Brandt, P., Stramma, L., and Schmidtko, S.: Drivers and mechanisms of ocean deoxygenation, Nat. Geosci., 11, 467–473, https://doi.org/10.1038/s41561-018-0152-2, 2018.

Peng, X. and Valentine, D. L.: Diversity and N_2O Production Potential of Fungi in an Oceanic Oxygen Minimum Zone, J. Fungi, 7, 218, https://doi.org/10.3390/jof7030218, 2021.

Popp, B. N., Westley, M. B., Toyoda, S., Miwa, T., Dore, J. E., Yoshida, N., Rust, T. M., Sansone, F. J., Russ, M. E., Ostrom, N. E., and Ostrom, P. H.: Nitrogen and oxygen isotopomeric constraints on the origins and sea-to-air flux of N_2O in the oligotrophic subtropical North Pacific gyre, Global Biogeochem. Cy., 16, 12-1–12-10, https://doi.org/10.1029/2001GB001806, 2002.

Rahn, T. and Wahlen, M.: A reassessment of the global isotopic budget of atmospheric nitrous oxide, Global Biogeochem. Cy., 14, 537–543, https://doi.org/10.1029/1999GB900070, 2000.

Rohe, L., Anderson, T.-H., Braker, G., Flessa, H., Giesemann, A., Lewicka-Szczebak, D., Wrage-Mönnig, N., and Well, R.: Dual isotope and isotopomer signatures of nitrous oxide from fungal denitrification – a pure culture study, Rapid Commun. Mass Sp., 28, 1893–1903, https://doi.org/10.1002/rcm.6975, 2014.

Schmidtko, S., Stramma, L., and Visbeck, M.: Decline in global oceanic oxygen content during the past five decades, Nature, 542, 335–339, https://doi.org/10.1038/nature21399, 2017.

Shoun, H., Fushinobu, S., Jiang, L., Kim, S.-W., and Wakagi, T.: Fungal denitrification and nitric oxide reductase cytochrome P450nor, Philos. Trans. Biol. Sci., 367, 1186–1194, 2012.

Si, Y., Zhu, Y., Sanders, I., Kinkel, D. B., Purdy, K. J., and Trimmer, M.: Direct biological fixation provides a freshwater sink for N_2O, Nat. Commun., 14, 6775, https://doi.org/10.1038/s41467-023-42481-2, 2023.

Sigman, D. M., Casciotti, K. L., Andreani, M., Barford, C., Galanter, M., and Böhlke, J. K.: A Bacterial Method for the Nitrogen Isotopic Analysis of Nitrate in Seawater and Freshwater, Anal. Chem., 73, 4145–4153, https://doi.org/10.1021/ac010088e, 2001.

Smith, C., Nicholls, Z. R. J., Armour, K., Collins, W., Dufresne, J.-L., Frame, D., Lunt, D. J., Mauritsen, M. D., Palmer, M. D., Watanabe, M., Wild, M., and Zhang, H.: The Earth's Energy Budget, Climate Feedbacks, and Climate Sensitivity Supplementary Material, in: Climate Change 2021: The Physical Science Basis, Contribution of Working Group I to the Sixth Assessment Report of the Intergovernmental Panel on Climate Change, edited by: Masson-Delmotte, V., Zhai, P., Pirani, A., Connors, S. L., Péan, C., Berger, S., Caud, N., Chen, Y., Goldfarb, L., Gomis, M. I., Huang, M., Leitzell, K., Lonnoy, E., Matthews, J. B. R., Maycock, T. K., Waterfield, T., Yelekçi, O., Yu, R., and Zhou, B., Cambridge University Press, Cambridge, United Kingdom, ISBN: 978-1-00-915789-6, https://doi.org/10.1017/9781009157896, 2021.

Smriga, S., Ciccarese, D., and Babbin, A. R.: Denitrifying bacteria respond to and shape microscale gradients within particulate matrices, Commun. Biol., 4, 570, https://doi.org/10.1038/s42003-021-02102-4, 2021.

Stein, L. Y.: Insights into the physiology of ammonia-oxidizing microorganisms, Curr. Opin. Chem. Biol., 49, 9–15, https://doi.org/10.1016/j.cbpa.2018.09.003, 2019.

Stein, L. Y. and Yung, Y. L.: Production, Isotopic Composition, and Atmospheric Fate of Biologically Produced Nitrous Oxide, Annu. Rev. Earth Pl. Sc., 31, 329–356, https://doi.org/10.1146/annurev.earth.31.110502.080901, 2003.

Stieglmeier, M., Mooshammer, M., Kitzler, B., Wanek, W., Zechmeister-Boltenstern, S., Richter, A., and Schleper, C.: Aerobic nitrous oxide production through N-nitrosating hybrid formation in ammonia-oxidizing archaea, ISME J., 8, 1135–1146, https://doi.org/10.1038/ismej.2013.220, 2014.

Stramma, L., Johnson, G. C., Sprintall, J., and Mohrholz, V.: Expanding Oxygen-Minimum Zones in the Tropical Oceans, Science, 320, 655–658, https://doi.org/10.1126/science.1153847, 2008.

Sun, X., Ji, Q., Jayakumar, A., and Ward, B. B.: Dependence of nitrite oxidation on nitrite and oxygen in low-oxygen seawater, Geophys. Res. Lett., 44, 7883–7891, https://doi.org/10.1002/2017GL074355, 2017.

Sun, X., Jayakumar, A., Tracey, J. C., Wallace, E., Kelly, C. L., Casciotti, K. L., and Ward, B. B.: Microbial N_2O consumption in and above marine N_2O production hotspots, ISME J., 15, 1434–1444, https://doi.org/10.1038/s41396-020-00861-2, 2021a.

Sun, X., Frey, C., Garcia-Robledo, E., Jayakumar, A., and Ward, B. B.: Microbial niche differentiation explains nitrite oxidation in marine oxygen minimum zones, ISME J., 15, 1317–1329, https://doi.org/10.1038/s41396-020-00852-3, 2021b.

Sutka, R. L., Ostrom, N. E., Ostrom, P. H., Gandhi, H., and Breznak, J. A.: Nitrogen isotopomer site preference of N_2O produced by Nitrosomonas europaea and Methylococcus capsulatus Bath, Rapid Commun. Mass Sp., 17, 738–745, https://doi.org/10.1002/rcm.968, 2003.

Sutka, R. L., Ostrom, N. E., Ostrom, P. H., Gandhi, H., and Breznak, J. A.: Nitrogen isotopomer site preference of N_2O produced by Nitrosomonas europaea and Methylococcus capsulatus Bath, Rapid Commun. Mass Sp., 18, 1411–1412, https://doi.org/10.1002/rcm.1482, 2004.

Sutka, R. L., Ostrom, N. E., Ostrom, P. H., Breznak, J. A., Gandhi, H., Pitt, A. J., and Li, F.: Distinguishing Nitrous Oxide Production from Nitrification and Denitrification on the Basis of Isotopomer Abundances, Appl. Environ. Microbiol., 72, 638–644, https://doi.org/10.1128/AEM.72.1.638-644.2006, 2006.

Sutka, R. L., Adams, G. C., Ostrom, N. E., and Ostrom, P. H.: Isotopologue fractionation during N_2O production by fungal denitrification, Rapid Commun. Mass Sp., 22, 3989–3996, https://doi.org/10.1002/rcm.3820, 2008.

Tian, H., Xu, R., Canadell, J. G., Thompson, R. L., Winiwarter, W., Suntharalingam, P., Davidson, E. A., Ciais, P., Jackson, R. B., Janssens-Maenhout, G., Prather, M. J., Regnier, P., Pan, N., Pan, S., Peters, G. P., Shi, H., Tubiello, F. N., Zaehle, S., Zhou, F., Arneth, A., Battaglia, G., Berthet, S., Bopp, L., Bouwman, A. F., Buitenhuis, E. T., Chang, J., Chipperfield, M. P., Dangal, S. R. S., Dlugokencky, E., Elkins, J. W., Eyre, B. D., Fu, B., Hall, B., Ito, A., Joos, F., Krummel, P. B., Landolfi, A., Laruelle, G. G., Lauerwald, R., Li, W., Lienert, S., Maavara, T., MacLeod, M., Millet, D. B., Olin, S., Patra, P. K., Prinn, R. G., Raymond, P. A., Ruiz, D. J., van der Werf, G. R., Vuichard, N., Wang, J., Weiss, R. F., Wells, K. C., Wilson, C., Yang, J., and Yao, Y.: A comprehensive quantification of global nitrous oxide sources and sinks, Nature, 586, 248–256, https://doi.org/10.1038/s41586-020-2780-0, 2020.

Toyoda, S. and Yoshida, N.: Determination of nitrogen isotopomers of nitrous oxide on a modified isotope ratio mass spectrometer, Anal. Chem., 71, 4711–4718, https://doi.org/10.1021/ac9904563, 1999.

Toyoda, S., Yoshida, N., Miwa, T., Matsui, Y., Yamagishi, H., Tsunogai, U., Nojiri, Y., and Tsurushima, N.: Production mechanism and global budget of N_2O inferred from its isotopomers in the western North Pacific, Geophys. Res. Lett., 29, 7-1–7-4, https://doi.org/10.1029/2001GL014311, 2002.

Toyoda, S., Mutobe, H., Yamagishi, H., Yoshida, N., and Tanji, Y.: Fractionation of N_2O isotopomers during production by denitrifier, Soil Biol. Biochem., 37, 1535–1545, https://doi.org/10.1016/j.soilbio.2005.01.009, 2005.

Toyoda, S., Yoshida, O., Yamagishi, H., Fujii, A., Yoshida, N., and Watanabe, S.: Identifying the origin of nitrous oxide dissolved in deep ocean by concentration and isotopocule analyses, Sci. Rep., 9, 1–9, https://doi.org/10.1038/s41598-019-44224-0, 2019.

Toyoda, S., Kakimoto, T., Kudo, K., Yoshida, N., Sasano, D., Kosugi, N., Ishii, M., Kameyama, S., Inagawa, M., Yoshikawa-Inoue, H., Nishino, S., Murata, A., Ishidoya, S., and Morimoto, S.: Distribution and Production Mechanisms of N_2O in the Western Arctic Ocean, Global Biogeochem. Cy., 35, e2020GB006881, https://doi.org/10.1029/2020GB006881, 2021.

Toyoda, S., Terajima, K., Yoshida, N., Yoshikawa, C., Makabe, A., Hashihama, F., and Ogawa, H.: Extensive Accumulation of Nitrous Oxide in the Oxygen Minimum Zone in the Bay of Bengal, Global Biogeochem. Cy., 37, e2022GB007689, https://doi.org/10.1029/2022GB007689, 2023.

Travis, N. M., Kelly, C. L., Mulholland, M. R., and Casciotti, K. L.: Nitrite cycling in the primary nitrite maxima of the eastern tropical North Pacific, Biogeosciences, 20, 325–347, https://doi.org/10.5194/bg-20-325-2023, 2023.

Trimmer, M., Chronopoulou, P.-M., Maanoja, S. T., Upstill-Goddard, R. C., Kitidis, V., and Purdy, K. J.: Nitrous oxide as a function of oxygen and archaeal gene abundance in the North Pacific, Nat. Commun., 7, 13451–13451, https://doi.org/10.1038/ncomms13451, 2016.

Vajrala, N., Martens-Habbena, W., Sayavedra-Soto, L. A., Schauer, A., Bottomley, P. J., Stahl, D. A., and Arp, D. J.: Hydroxylamine as an intermediate in ammonia oxidation by globally abundant marine archaea, P. Natl. Acad. Sci. USA, 110, 1006–1011, 2013.

Virtanen, P., Gommers, R., Oliphant, T. E., Haberland, M., Reddy, T., Cournapeau, D., Burovski, E., Peterson, P., Weckesser, W., Bright, J., van der Walt, S. J., Brett, M., Wilson, J., Millman, K. J., Mayorov, N., Nelson, A. R. J., Jones, E., Kern, R., Larson, E., Carey, C. J., Polat, İ., Feng, Y., Moore, E. W., VanderPlas, J., Laxalde, D., Perktold, J., Cimrman, R., Henriksen, I., Quintero, E. A., Harris, C. R., Archibald, A. M., Ribeiro, A. H., Pedregosa, F., and van Mulbregt, P.: SciPy 1.0: fundamental algorithms for scientific computing in Python, Nat. Method., 17, 261–272, https://doi.org/10.1038/s41592-019-0686-2, 2020.

Wan, X. S., Sheng, H.-X., Liu, L., Shen, H., Tang, W., Zou, W., Xu, M. N., Zheng, Z., Tan, E., Chen, M., Zhang, Y., Ward, B. B., and Kao, S.-J.: Particle-associated denitrification is the primary source of N_2O in oxic coastal waters, Nat. Commun., 14, 8280, https://doi.org/10.1038/s41467-023-43997-3, 2023a.

Wan, X. S., Hou, L., Kao, S.-J., Zhang, Y., Sheng, H.-X., Shen, H., Tong, S., Qin, W., and Ward, B. B.: Pathways of N_2O production by marine ammonia-oxidizing archaea determined from dual-isotope labeling, P. Natl. Acad. Sci. USA, 120, e2220697120, https://doi.org/10.1073/pnas.2220697120, 2023b.

Wang, R. Z., Lonergan, Z. R., Wilbert, S. A., Eiler, J. M., and Newman, D. K.: Widespread detoxifying NO reductases impart a distinct isotopic fingerprint on N $_2$O under anoxia, Microbiology, bioRxiv 2023.10.13.562248, https://doi.org/10.1101/2023.10.13.562248, 2023.

Wei, J., Ibraim, E., Brüggemann, N., Vereecken, H., and Mohn, J.: First real-time isotopic characterisation of N_2O from chemodenitrification, Geochim. Cosmochim. Ac., 267, 17–32, https://doi.org/10.1016/j.gca.2019.09.018, 2019.

Westley, M. B., Yamagishi, H., Popp, B. N., and Yoshida, N.: Nitrous oxide cycling in the Black Sea inferred from stable isotope and isotopomer distributions, Deep-Sea Res. Pt. II, 53, 1802–1816, https://doi.org/10.1016/j.dsr2.2006.03.012, 2006.

Wrage, N., Velthof, G. L., Van Beusichem, M. L., and Oenema, O.: Role of nitrifier denitrification in the production of nitrous oxide, Soil Biol. Biochem., 33, 1723–1732, https://doi.org/10.1016/S0038-0717(01)00096-7, 2001.

Yamagishi, H., Westley, M. B., Popp, B. N., Toyoda, S., Yoshida, N., Watanabe, S., Koba, K., and Yamanaka, Y.: Role of nitrification and denitrification on the nitrous oxide cycle in the eastern tropical North Pacific and Gulf of California, J. Geophys. Res.-Biogeo., 112, G02015, https://doi.org/10.1029/2006JG000227, 2007.

Yang, H., Gandhi, H., Ostrom, N. E., and Hegg, E. L.: Isotopic Fractionation by a Fungal P450 Nitric Oxide Reductase during the Production of N_2O, Environ. Sci. Technol., 48, 10707–10715, https://doi.org/10.1021/es501912d, 2014.

Zumft, W. G.: Cell biology and molecular basis of denitrification, Microbiol. Mol. Biol. Rev., 61, 533–616, https://doi.org/10.1128/mmbr.61.4.533-616.1997, 1997.